FGF pathway overactivation underlies reduced neurogenesis in cerebellar organoid models of neurodevelopmental ciliopathy

Ludovica Brunetti[1,2,*], Antonia Wiegering[1,2], Isabelle Anselme[1,2], Lidia Pollara[3,4], Martin Catala[1,2], Christophe Antoniewski[2], Enza Maria Valente[3,4], Sylvie Schneider-Maunoury[1,2,#,*], Christine Vesque[1,2,#,*]

1. Sorbonne Université, CNRS, Inserm, Development, Adaptation and Aging, Dev2A, F-75005 Paris, France
2. Sorbonne Université, CNRS, Inserm, Institut de Biologie Paris Seine, IBPS, F-75005 Paris, France
3. Department of Molecular Medicine, University of Pavia, Pavia, Italy
4. Neurogenetics Research Center, IRCCS Mondino Foundation, Pavia, Italy

# These authors jointly supervised this work

* co-corresponding authors

ABSTRACT

Cerebellar hypoplasia and dysplasia are hallmark features of neurodevelopmental ciliopathies such as Joubert syndrome. These disorders are caused by biallelic mutations in genes regulating the function of the primary cilium, a near-ubiquitous antenna-like organelle involved in signal reception and transduction. However, the pathogenetic mechanisms linking ciliary gene dysfunction to Joubert syndrome neurodevelopmental defects are poorly understood. Here, we generate cerebellar organoids from human induced pluripotent stem cells carrying either null mutations or patient-derived variants in *RPGRIP1L*, a Joubert syndrome-associated gene encoding a scaffold protein crucial for ciliary function. While control organoids robustly express markers of cerebellar glutamatergic and GABAergic lineages including Purkinje cells, *RPGRIP1L*-deficient organoids display a consistent and severe reduction in Purkinje cell markers, accompanied by impaired neurogenesis and increased progenitor proliferation. These defects coincide with prolonged overactivation of the FGF/MAPK signaling pathway, consistent with the enrichment of MEK1/2 pathway effector at cilia base. Pharmacological inhibition of FGF receptors reduces MEK1/2 activation at cilia base and rescues both the proliferative-neurogenic balance and Purkinje lineage formation in *RPGRIP1L*-deficient organoids. Together, our findings reveal FGF/MAPK signaling modulation at the ciliary base in neural progenitors and identify early FGF pathway overactivation as a key driver of cerebellar differentiation defects in an *in vitro* human model of Joubert syndrome. This provides new insight into the developmental origin of cerebellar impairment in neurodevelopmental ciliopathies.

INTRODUCTION

Cerebellar dysfunction is a common feature of several developmental disorders, associated with both motor disease and cognitive impairment [1]. The cerebellum originates from dorsal hindbrain rhombomere 1 (r1) under inductive cues from the isthmic organizer at the midbrain–hindbrain boundary, where fibroblast growth factor 8 (FGF8) expression defines the early cerebellar territory [2–4]. Two distinct germinal zones subsequently form: the ventricular zone (VZ), which produces inhibitory GABAergic neurons such as Purkinje, Golgi, and basket cells [5], and the rhombic lip (RL), which generates excitatory glutamatergic lineages including granule neurons (GNs) and unipolar brush cells [6,7]. In humans, Purkinje cell neurogenesis occurs between post-conception weeks (PCW) 8–10 [8,9], whereas granule cell progenitors (GCPs) proliferate extensively around 26 PCW [10]. Coordinated proliferation and differentiation of these populations are critical for establishing cerebellar size, morphology, and function [11].

Joubert syndrome (JBTS) is a rare neurodevelopmental disease affecting the cerebellum and brainstem, primarily characterized by hypoplasia/dysplasia of the vermis – the medial cerebellar structure. All JBTS patients share the diagnostic “molar tooth sign” on axial brain imaging, resulting from specific cerebellar and brainstem malformations [12,13]. Clinically, patients present with ataxia, ocular motor defects, developmental delay, and intellectual disability [14]. Over 40 causative genes have been identified, all encoding proteins involved in primary cilia structure or function [13,15]. Primary cilia are microtubular sensory organelles protruding from the surface of almost all vertebrate cells, acting as signaling hubs [16–18]. To ensure proper signaling their composition is controlled by the transition zone, composed of protein complexes such as the MKS, NPHP (NPHP1, NPHP4, NPHP8/RPGRIP1L), and CEP290 modules [19,20]. Among them, the JBTS gene *RPGRIP1L* encodes a scaffolding protein essential for transition zone integrity [21,22] and HH pathway activity [23,24]. Mutations in *RPGRIP1L* can also cause the more severe Meckel syndrome [25].

In the cerebellum, ciliogenesis is temporally regulated to ensure appropriate responsiveness to SHH and other signals [26–28]. In mice, a loss of cilia in the brain causes cerebellar hypoplasia and foliation defects due to loss of SHH-dependent GCP proliferation [29,30], while mouse

96 mutants for JBTS genes — including *Rpgrip1l* [25], *Ahi1* [31], *Tmem67* [32], *Jbts17 (CPLANE1)* [33],
97 *Talpid3* [34], *Arl13b* [35] and Cep290 [31] — exhibit variable cerebellar phenotypes and divergent
98 effects on HH and WNT signaling. In humans, the analysis of JBTS fetal samples with a
99 confirmed diagnosis of cerebellar vermis hypoplasia revealed a reduction of GCP proliferation
100 associated with a lower expression of HH targets, with no differences between hemispheres
101 and vermis. These findings suggest that the specific vermis hypoplasia observed in JBTS
102 patients precedes and is independent of GCP proliferation defects, leaving its primary origin
103 unresolved [36]. Overall, the pathogenetic mechanisms linking cilia dysfunction to JBTS
104 neurodevelopmental defects remain largely unknown and may be of diverse origins.
105
106 This leaves us with several open questions: i) what are the early cellular and molecular
107 processes affected by JBTS gene depletion during human cerebellar development? ii) can
108 some of these defects account for cerebellar vermis hypo/dysplasia observed in JBTS patients?
109 iii) can we identify drug treatments that could potentially alleviate JBTS disease
110 manifestations? In order to address these questions, we turned to human iPSC-derived
111 cerebellar organoids, recently established as promising approaches to study human cerebellar
112 development and neurodevelopmental diseases [37–44]. By recapitulating developmental
113 pathways, these approaches are particularly well suited to study early steps of cerebellar
114 development. Moreover, in a previous work we demonstrated significant differences
115 concerning cilia formation and function in human and mouse spinal organoids in the absence
116 of JBTS proteins (RPGRIP1L and TMEM67) [45], further emphasizing the importance of using
117 human-based systems to investigate the developmental origin of cilia-related cerebellar
118 defects.
119
120 Here, we employ human iPSC-derived cerebellar organoids to investigate the role of *RPGRIP1L*
121 in cerebellar development, given its central role in ciliary transition zone assembly and the
122 severe neurodevelopmental defects reported in mouse models [46]. Using organoids derived
123 from JBTS patient iPSCs carrying biallelic *RPGRIP1L* mutations and CRISPR-engineered
124 knockouts, we uncover early ciliary abnormalities, morphological alterations, and aberrant
125 FGF/MAPK signaling activation, including increased levels of phosphorylated pathway
126 effector MEK1/2 at the ciliary base. Excessive FGF activity drives progenitor hyperproliferation

127 and impaired neurogenesis, defects that are rescued by pharmacological inhibition of the FGF
128 pathway after midbrain-hindbrain boundary induction.
129 Our findings reveal a causal link between *RPGRIP1L* dysfunction, dysregulated FGF signaling,
130 and disrupted cerebellar neurogenesis, providing mechanistic insight into the developmental
131 origin of cerebellar malformations in JBTS.

132 **RESULTS**

133

134 ***Cerebellar organoids generated from human induced pluripotent stem cells recapitulate***
135 ***early steps of cerebellar development***

136 To unravel molecular mechanisms and biological processes that may be responsible for
137 cerebellar defects in JBTS pathogenesis, we used organoids to model early stages of human
138 cerebellar development *in vitro*. We optimized published protocols for generating cerebellar
139 organoids from human induced pluripotent stem cells (hiPSCs) [37,39]. To induce neural
140 commitment, mid-hindbrain boundary establishment and tissue self-organization, embryoid
141 bodies were sequentially treated with fibroblast growth factor 2 (FGF2), insulin, TGFß/SMAD
142 inhibitor (SB431542), FGF19 and stromal cell-derived factor 1 (SDF1) (**Fig. 1A).** Since dynamic
143 culture conditions have been shown to favor faster cerebellar commitment [47], embryoid
144 bodies were cultured under orbital agitation from day 7 onwards.

145 Immunostaining analysis on control organoid cryosections showed clusters of neural
146 progenitors ($SOX2^+$) and early-born neurons (HUC/D^+), already present at day 14
147 (**Supplementary Fig. 1A**), progressively expanding and self-organizing (**Supplementary Fig.**
148 **1A-C**). By day 28, early-born neurons are primarily located in deep regions of the organoid
149 tissue, adjacent to an outer layer of neural progenitors organized either at the organoid
150 periphery or into small internal rosettes (**Supplementary Fig. 1C**).

151 To assess the time-course of cerebellar cell type production in our experimental settings, we
152 performed bulk RNAseq analysis on cerebellar organoids derived from two independent
153 control hiPSC lines with different genetic backgrounds, PCIi033-A (Ph2) and UCSFi001-A
154 (Wtc11) at the hiPSC stage (day 0) and at five timepoints of the differentiation protocol (day
155 7, 14, 21, 28, 35) (see **Supplementary Excel File 1** for normalized gene expression data). First,
156 we validated that the control organoids faithfully recapitulated early stages of cerebellar
157 development, with the presence of midbrain, hindbrain and mid-hindbrain boundary markers
158 and the absence of anterior forebrain and posterior hindbrain markers **(Figure 1C)**. Concerning
159 cerebellar differentiation, the order of appearance of GABAergic Purkinje lineage markers
160 reflected the *in vivo* maturation stages of this cell population, with the progenitor marker
161 *OLIG2* and the early post-mitotic marker *SKOR2* peaking at day 21, followed by the more
162 mature Purkinje marker *CALB1*, strongly expressed between day 28 and 35 **(Supplementary**
163 **Fig 1D)**. As for the glutamatergic lineage, the RNA levels of progenitor markers were gradually

164 increased over time, first appearing at day 7 for *PAX6* and *BARHL1*, and at day 14 for *ATOH1*
165 **(Supplementary Fig. 1E**). Of note, the mature GN marker, *GABRA6*, was not detected over the
166 35 days short-term organoid culture, consistent with its post-natal onset in humans [9,48]
167 **(Supplementary Fig. 1F)**. Given the well-established role of the SHH pathway in GCP pool
168 expansion during cerebellar development [49,30], we also examined SHH ligand expression.
169 However, almost no *SHH* mRNA was detected over the 35 days of cerebellar differentiation
170 **(Supplementary Fig. 1G)**. Immunostaining analysis showed that the GCP marker BARHL1 and
171 the Purkinje marker CALB1 segregated in separated domains within the organoid tissue, with
172 few cells intermingled **(Supplementary Fig. 1H)**.
173 Altogether these data provide strong evidence for self-organization of a cerebellar
174 primordium and successful specification of the two main cerebellar lineages following our
175 differentiation protocol. They also show that this 35-days differentiation protocol models early
176 cerebellar developmental stages, preceding SHH endogenous expression by Purkinje cells.
177
178 ***RPGRIP1L KO and JBTS patient-derived cerebellar organoids present a severe reduction of***
179 ***Purkinje Cell markers and a milder decrease in Granule Cell Progenitor markers***
180 To compare the differentiation process between healthy and JBTS pathological conditions, we
181 used two independent *RPGRIP1L* KO hiPSC lines – generated in the two different genetic
182 backgrounds previously used for control organoid analysis (Ph2 and Wtc11) [45] – both
183 producing early truncated proteins within the first coiled coil domain **(Fig. 1B)**. In parallel we
184 also analyzed a hiPSC line derived from a severely affected JBTS patient (NG2266) carrying two
185 pathogenic variants in the *RPGRIP1L* gene (p.Q684X/c.2304+1G>T) [50] **(Fig. 1B)**. Both variants
186 of this patient are predicted by VarSome to be null variants and are classified as pathogenic
187 following the pathogenicity criterium "very strong" (PVS1) accordingly to the ACMG
188 (American College of Medical Genetics and Genomics) standards and guidelines [51] and encode
189 truncated proteins missing the second C2 domain and C-terminal RPGR-Interacting domain
190 (RID) of the protein (see Methods and **Supplementary Fig. 6**). We generated cerebellar
191 organoids from both *RPGRIP1L* KO hiPSC lines (Ph2 and Wtc11) in parallel with their isogenic
192 controls, and from the JBTS patient-derived hiPSC line (NG2266).
193 Using a specific antibody raised against the human RPGRIP1L RID domain, we showed the
194 presence of RPGRIP1L protein at its subcellular localization at the ciliary transition zone in

195 control organoids (**Supplementary Fig. 2A, A'**). On the contrary, no signal was detected in cilia
196 from both *RPGRIP1L* KO and JBTS patient-derived organoids (**Supplementary Fig. 2B-C'**).
197 Bulk RNAseq analysis was performed on hiPSC cells and on cerebellar organoids collected
198 every seven days from day 7 to day 35 from several independent experiments (see
199 **Supplementary Excel File 1** for normalized gene expression data). We showed that both
200 *RPGRIP1L* KO and JBTS patient-derived organoids at day 7 expressed mid-hindbrain markers,
201 while being negative for anterior forebrain and caudal hindbrain markers **(Fig 1C),** thus
202 showing proper specification of their early anteroposterior identity. However, JBTS patient-
203 derived organoids displayed lower levels of WNT1 and EN1 than controls (**Fig. 1C**).
204 From day 14 onwards, transcriptome analysis revealed a consistent and severe reduction of
205 numerous Purkinje markers (*OLIG2, SKOR2, CALB1, FOXP2, PDE1C, ITPR1*) in both *RPGRIP1L*
206 KO and JBTS patient-derived organoids compared to controls **(Fig. 1D, Supplementary Fig. 2D)**.
207 Quantitative PCR analysis corroborated these results showing a significant decrease of *OLIG2,*
208 *SKOR2* and *CALB1* markers in *RPGRIP1L* KO organoids derived from both hiPSC lines and in
209 JBTS patient-derived organoids, compared to controls **(Supplementary Fig. 2E)**.
210 In contrast, the expression levels of the glutamatergic lineage markers *ATOH1* and *BARHL1*
211 were not consistently affected across *RPGRIP1L*-deficient conditions compared to controls
212 **(Figure 1E)**. This was confirmed by quantitative PCR analysis where the only significant defects
213 were a decrease in *BARHL1* expression in JBTS patient-derived organoids and an increase in
214 ATOH1 expression in *RPGRIP1L* KO organoids at d35 **(Supplementary Fig. 2F**).
215 In order to strengthen these findings, we assayed protein expression of both Purkinje lineage
216 markers (OLIG2, CALB1) and glutamatergic lineage markers (ATOH1, BARHL1) by quantifying
217 the number of positive cells after immunostaining on organoid cryosections. Each marker was
218 analyzed at the timepoint of its highest expression in control organoids, as determined by bulk
219 RNA-seq data: day 21 for OLIG2 and day 28 for CALB1, ATOH1, and BARHL1. OLIG2- and CALB1-
220 positive cells were barely detected in *RPGRIP1L* KO and JBTS patient-derived organoids, while
221 strong and widespread labeling was observed in control organoids (**Fig. 1F-I, Supplementary**
222 **Fig. 2I**). Regarding the glutamatergic lineage, the number of BARHL1 positive cells was reduced
223 by 50% in *RPGRIP1L* KO and JBTS patient-derived organoids, along with a decrease in the
224 average labeling intensity of individual cells (**Fig. 1J, K, Supplementary Fig. 2J**). The number of
225 ATOH1 positive cells was only reduced in JBTS patient organoids (**Supplementary Fig. 2G, H)**

226 whereas the intensity of ATOH1 labelling was reduced by ~50% both in JBTS patient and
227 *RPGRIP1L* KO conditions (**Supplementary Fig. 2K**).
228 Overall, these data indicate a severe and significant impairment in the specification and
229 production of the Purkinje lineage in all *RPGRIP1L*-deficient conditions from day 21 onwards,
230 whereas glutamatergic lineage specification appeared to be modestly affected, mainly at
231 protein level from day 28.
232
233 ***Increased proportion of early neural progenitors in RPGRIP1L KO and JBTS patient cerebellar***
234 ***organoids***
235 We assessed whether these molecular alterations observed upon *RPGRIP1L* impairment might
236 be preceded by earlier defects in tissue organization. The first obvious morphological
237 alteration under brightfield observation was a size increase of *RPGRIP1L* KO and JBTS patient
238 organoids compared to controls, from day 21 onward **(Fig. 2A)**. Organoid area was measured
239 every 7 days along the differentiation protocol in several independent experiments. At day 28
240 and 35, both *RPGRIP1L* KO and JBTS patient-derived organoids presented a significant area
241 increase compared to controls (3.3-fold for *RPGRIP1L* KO and 2.3-fold for JBTS patient-derived
242 organoids over controls at day 35) **(Fig. 2B)**.
243 Moreover, the general tissue organization was already perturbed at day 14, before overt size
244 increase. In control organoids, early polarized neural progenitors ($SOX2^+/ZO1^+$) formed few
245 internal rosettes **(Fig. 2C left panels)**. By contrast, *RPGRIP1L* KO (Ph2 and Wtc11 lines) and
246 JBTS patient-derived organoids exhibited a higher number of internal rosettes. Additionally, in
247 all *RPGRIP1L*-deficient conditions, polarized neural progenitors ($SOX2^+/ZO1^+$) extended across
248 the entire organoid surface, with their apical side oriented outward, forming a continuous
249 neuroepithelium in contact with the medium **(Fig. 2C, middle and right panels)**.
250 The area occupied by ZO1 apical surface within the organoid was expanded by 12-fold in
251 *RPGRIP1L*-KO (Ph2 and Wtc11 lines) and by 15-fold in JBTS patient-derived organoids
252 compared to control condition at day 14 **(Fig. 2D).** Similarly, the number of SOX2+ neural
253 progenitors was doubled in all *RPGRIP1L*-deficient conditions compared to controls **(Fig. 2E)**.
254
255 ***Differential dependence on RPGRIP1L protein among neural progenitors for ciliogenesis***
256 Given the well-established role of *RPGRIP1L* in building functional cilia [21,52,22] and the fact that
257 apical progenitors of the neural tube are ciliated [53–56], we investigated whether ciliogenesis

258 was affected in human cerebellar organoids. Immunostaining for the axonemal marker INPP5E
259 and for the basal body marker gamma-TUBULIN revealed numerous cilia pointing towards the
260 internal lumen of neural rosettes in both controls **(Fig. 3A, A')** and all *RPGRIP1L*-deficient
261 conditions **(Fig. 3B-C')**. Some cilia in *RPGRIP1L* KO and JBTS rosettes displayed a bulbous tip
262 **(Fig. 3B', C')**, a condition which was never observed in control rosettes. However, ciliary length
263 was not significantly changed in *RPGRIP1L* KO rosettes and only mildly decreased in JBTS
264 condition **(Fig. 3D)**.
265 In contrast, the analysis of non-polarized regions, characterized by random nuclear orientation
266 and distribution of gamma-TUBULIN+ basal bodies **(Fig. 3E-G)**, revealed a significant reduction
267 in the number of ciliated basal bodies in *RPGRIP1L*-deficient conditions (58% in *RPGRIP1L*-KO
268 and 47% in JBTS patient organoids, versus 85% in controls) **(Fig. 3H).** Moreover, ciliary length
269 increased **(Fig. 3I)** and INPP5E labeling intensity inside cilia was reduced **(Fig. 3J)**. Altogether
270 these results indicate an impaired ciliogenesis and altered ciliary trafficking in *RPGRIP1L*-
271 depleted non-polarized cells. Consistent with the literature indicating a cell type-specific
272 requirement for *RPGRIP1L* at the ciliary transition zone [52], our findings suggest that, in
273 cerebellar organoids*, RPGRIP1L* is necessary for both proper ciliogenesis and ciliary content in
274 non-polarized neural progenitors, while it appears dispensable for ciliogenesis in $ZO1^+$ early
275 human cerebellar progenitors at day 14. Nevertheless, the observation of numerous bulbous
276 tips on cilia of apical progenitors suggests that they might present an abnormal content, likely
277 to modify their signaling properties.
278
279 ***RPGRIP1L loss leads to neurogenesis impairment and transcriptional upregulation of FGF***
280 ***pathway genes***
281 In order to identify specific molecular pathways disrupted upon RPGRIP1L depletion we
282 performed a DESeq2 analysis on our bulk RNAseq dataset, comparing both *RPGRIP1L* KO and
283 JBTS patient-derived organoids with controls at selected timepoints.
284 At day 14, many genes appeared deregulated in both *RPGRIP1L* KO (2146 genes, P adj <0.05,
285 |log2FC|>1) and JBTS patient-derived organoids (4304 genes, P value <0.05, |log2FC|>1)
286 compared to controls (**Supplementary Excel Files 2 and 3,** respectively). The Volcano plots
287 representing significant DEGs (P value <0.05, |log2FC|>1) for *RPGRIP1L* KO compared to
288 control **(Fig. 4A)** or JBTS patient compared to control **(Fig. 4B)** revealed many genes commonly
289 de-regulated in both RPGRIP1L-deficient conditions. Among the most downregulated genes

290 were neurogenic master genes – *NEUROG1*, *NEUROD1* and *NEUROD4* – as well as other genes
291 involved in neurogenesis and early-born neuron functions like *HES6* [57,58], *GDNF* and *RELN* (**Fig.**
292 **4A, B**). On the contrary, several SOX and HES transcription factors, important to maintain a
293 neural progenitor state, were significantly up-regulated in both RPGRIP1L KO and JBTS patient-
294 derived organoids compared to controls (**Fig. 4A, B**). Most importantly, FGF signaling emerged
295 as a severely disrupted pathway, with many FGF ligands (FGF8, FGF19, FGF17) and
296 downstream targets (ETV4, ETV5, SPRY1-2-4, SP8) strongly up-regulated in both *RPGRIP1L* KO
297 and JBTS patient-derived organoids **(Fig.4A, B)**. In particular, *FGF8* emerged as the top up-
298 regulated FGF ligand gene, with a peak of maximal over-expression at day 14 in *RPGRIP1L* KO
299 organoids (log2FC=4.07, p adj=7.10E-30) and JBTS patient organoids (log2FC=6.01, p
300 adj=3.24E-32). Real-time quantitative PCR analysis of FGF8 expression confirmed this up-
301 regulation between day 14 and day 21 in *RPGRIP1L* KO and JBTS patient conditions versus
302 controls and a more exacerbate phenotype in JBTS patient organoids **(Fig. 4C).** To illustrate the
303 reproducibility of the differentiation protocol as well as the similarity of transcriptional
304 changes between *RPGRIP1L* KO and JBTS patient-derived organoids, we generated a heatmap
305 representation of normalized RNA expression values for selected genes over time **(Fig. 4D)**.
306 This showed that, in control samples, neurogenesis genes started to be expressed around day
307 14, concomitant with a downregulation of early progenitor marker genes. In *RPGRIP1L*-
308 deficient conditions, these changes were delayed or absent. Moreover, while in control
309 organoids FGF signaling peaked at day 7 and was turned off by day 14, in both *RPGRIP1L* KO
310 and JBTS patient-derived organoids this signaling was upregulated and longer maintained
311 (until day 21). Overall, these data suggest that the failure to down-regulate FGF signaling after
312 midbrain-hindbrain boundary specification in *RPGRIP1L*-deficient conditions may prevent
313 neurogenesis by maintaining early neural cells in their progenitor state.
314
315 ***FGF/MAPK pathway overactivation manifests as an increased number of SP8-expressing***
316 ***cells and by pMEK1/2 enrichment at the ciliary base***
317 To better characterize the upregulation of FGF signaling, we first investigated in which cells
318 FGF targets were upregulated. We performed immunofluorescence on organoid cryosections
319 for the transcription factor SP8, a known target of FGF8 in the brain [59–61]. In *RPGRIP1L* KO and
320 in JBTS patient-derived organoids, the number of SP8-expressing cells was increased by 5.7-
321 fold and 4.4-fold, respectively **(Fig. 4E).** Increased SP8 expression was found mostly, but not

322 only, on polarized progenitor cells of the organoid borders and internal rosettes. We then
323 assessed which cells were producing the FGF8 ligand. Immunostaining analysis on
324 cryosections of day 14 organoids revealed that the strongest FGF8 signal coincided with the
325 apical surfaces of early $SOX2^{+}/ZO1^{+}$ apical progenitors **(Supplementary Fig. 3)**. While in control
326 organoids we could only detect FGF8 protein in cells bordering the few internal lumens
327 **(Supplementary Fig. 3A)**, in *RPGRIP1L* KO and JBTS patient-derived organoids, FGF8
328 distribution was more widespread. Indeed, FGF8 was enriched on both the apical sides of
329 neural progenitors forming internal lumens **(Supplementary Fig. 3A)** and the external layer
330 covering the organoid surface **(Supplementary Fig. 3B)**. Thus, the upregulation of FGF
331 signaling observed in transcriptomic experiments may relate both to an increased number of
332 cells expressing the FGF8 ligand and to an increased response of downstream pathway targets
333 such as SP8, also known to activate FGF8 expression [59,60]. To link the FGF pathway upregulation
334 to cilia defects, we analyzed the subcellular localization of pathway members. FGFR1 and
335 FGFR2 and downstream MAPK pathway effectors have recently been reported to be localized
336 at the cilium of epithelial cells in culture [62]. While we could not detect ciliary FGFR localization
337 with available antibodies in our organoids, we found that an activated form of MEK1/2
338 (pMEK1/2), a MAPK pathway effector, localized at the cilium base in cerebellar organoid
339 cryosections at day 14. More precisely, pMEK1/2 was detected between the centriole labelled
340 with gamma-TUBULIN and the axoneme labelled by ARL13B, thus possibly at the transition
341 zone **(Fig. 4F)**. This was the major site of pMEK1/2 localization in non-mitotic cells of organoids
342 from all genotypes analyzed **(Supplementary Fig. 3C)**. In *RPGRIP1L* KO and JBTS patient-
343 derived organoids, pMEK1/2 localized to the distal end of centrioles even in the absence of an
344 axoneme and showed a global increase in intensity compared to controls, although levels
345 varied between organoids. **(Fig. 4F).** Thus, the loss of RPGRIP1L increased the activity of the
346 core FGF/MAPK signaling effector pMEK1/2 at the cilium base during cerebellar organoid
347 differentiation, showing FGF pathway overactivation within individual cells.
348
349 ***RPGRIP1L-deficient organoids display severe neuronal maturation and extracellular matrix***
350 ***defects***
351 To assess whether the impaired neurogenesis observed at early differentiation stages (day 14)
352 prevented the acquisition of a mature neuronal signature in *RPGRIP1L*-deficient conditions,
353 we analyzed DEG's profile at later stages. At day 28, we observed a significant downregulation

354 of numerous genes involved in neuronal maturation and function, both in *RPGRIP1L* KO and
355 JBTS patient conditions (**Supplementary Excel Files 4 and 5,** respectively) as illustrated by the
356 volcano plots **(Fig. 5A, B**) and on the heatmap representation of normalized RNA expression
357 values over time (**Fig. 5C, upper panel**). In absence of functional RPGRIP1L protein we also
358 observed a severe reduction of several genes encoding extracellular-matrix (ECM)
359 components, such as collagens and laminins, as well as integrin receptors **(Fig. 5A, B and Fig.**
360 **5C lower panel)**.
361 Gene ontology analyses performed to identify overrepresented gene categories in our DEG
362 lists corroborated these results. Indeed, the most significantly enriched GO terms among the
363 downregulated genes in both *RPGRIP1L* KO (**Fig 5D**) and JBTS patient (**Fig 5E**) conditions at day
364 28 included brain development, synaptic signaling/chemical synaptic transmission, regulation
365 of membrane potential/action potential, but also core matrisome and extracellular matrix
366 organization.
367 Altogether these results demonstrated a neuronal maturation impairment, following FGF
368 upregulation and neurogenesis defects at early stages, and highlighted a concomitant
369 transcriptional downregulation of major ECM components.
370
371 ***Blocking FGF signaling rescues neurogenesis and Purkinje cell progenitor markers in***
372 ***RPGRIP1L-deficient cerebellar organoids***
373 To test the hypothesis that the sustained and strong FGF signaling upon *RPGRIP1L* depletion
374 is at the origin of neurogenesis and neuronal differentiation impairment, we designed a drug
375 rescue experiment. Given that FGF8 expression is crucial for midbrain-hindbrain boundary
376 formation at early stages and that, in *RPGRIP1L*-deficient organoids, the over-expression of
377 FGF ligands and of their downstream targets started before day 14 and continued until day
378 21, we treated *RPGRIP1L*-deficient organoids (both KO and JBTS patient lines) with the pan-
379 FGFR inhibitor BGJ-398 (Infigratinib) [63], from day 11 to day 18 (**Fig. 6A**). Notably, BGJ-398
380 treatment restored a normal size of *RPGRIP1L*-KO and JBTS patient organoids (**Fig. 6B**).
381 We then performed bulk RNAseq analysis on the BGJ treated samples and compared them to
382 their untreated counterparts. Heatmap representation of normalized RNA expression values
383 for selected genes over time clearly show that BGJ treatment was able to rescue the
384 expression of FGF pathway related genes, as well as neurogenesis, neuronal differentiation
385 and extracellular matrix genes in both RPGRIP1L KO **(Fig. 6C and Supplementary Fig. 4A)** and

386 JBTS patient organoids **(Fig. 6D and Supplementary Fig. 4B)** from several independent
387 experiments (see **Supplementary Excel File 6** for normalized gene expression data)**.**
388 Quantitative PCR analysis confirmed these results: the RNA expression levels of *FGF8* and its
389 downstream targets (*ETV4, ETV5, SPRY1*) were completely restored by the drug treatment in
390 both RPGRIP1L KO and JBTS patient organoids at all timepoints analyzed **(Supplementary Fig.**
391 **4C-F)**. The expression levels of proneural genes *NEUROG1* and *NEUROD1*, as well as Purkinje
392 markers *SKOR2* and *CALB1*, analyzed by quantitative PCR were partially rescued in *RPGRIP1L*
393 KO and JBTS patient organoids upon BGJ-398 treatment, in particular at their peak of
394 expression (**Supplementary Fig. 4G-J**). Immunofluorescence analysis on cryosections of day
395 14 organoids corroborated these results, showing a significant rescue in the number of
396 positive nuclei for either NEUROD1, HUC/D or SOX2 markers, upon BGJ-398 treatment in both
397 *RPGRIP1L* KO or JBTS patient-derived organoids (**Fig. 6E-H**). The expression level of the
398 Purkinje progenitor marker OLIG2 was also significantly rescued upon BGJ-398 treatment in
399 both *RPGRIP1L* KO and JBTS patient-derived organoids, as shown by immunofluorescence
400 analysis at day 21 **(Supplementary Fig. 4K).**
401 To confirm that BGJ-398 indeed acted on FGF signaling, we analyzed both targets and pathway
402 members by immunostaining on *RPGRIP1L* KO and JBTS patient-derived organoids with or
403 without drug treatment. BGJ treatment significantly reduced the number of SP8-expressing
404 cells in both *RPGRIP1L*-deficient conditions **(Fig 7A)**. In addition, pMEK1/2 amount at cilia
405 base was also significantly reduced by the drug treatment **(Fig. 7B)**.
406 Finally, to investigate whether reducing FGF signaling could act on cilia formation and content
407 in *RPGRIP1L*-deficient conditions, we analyzed cilia features in rescue experiments. We found
408 that BGJ-398 treatment had no impact on either cilia density **(Fig. 7C)**, cilia length **(Fig. 7D)** or
409 ciliary INPPP5E amount **(Fig. 7E)** in *RPGRIP1L* KO and in JBTS patient-derived organoids.
410 Thus, downregulating FGF signaling in *RPGRIP1L*-deficient cerebellar organoids efficiently
411 rescued the neurogenesis defect without rescuing cilia features.
412
413 ***Neural progenitor proliferation is increased in RPGRIP1L-deficient organoids and is rescued***
414 ***by blocking FGF signaling***
415 To test whether the size increase observed upon *RPGRIP1L* impairment could be due to
416 sustained proliferation caused by FGF overexpression, we assessed the proliferative potential
417 of neural progenitors in control, *RPGRIP1L* KO and JBTS patient-derived organoids by carrying

418 EdU pulse-chase experiments. We provided a 2h EdU pulse to the organoid cultures at day 18,
419 just before the onset of size increase. Some organoids were fixed 2h after the pulse. At this
420 stage (day 18), all *RPGRIP1L*-deficient organoids showed an increase of EdU positive cells
421 compared to controls (1.6-fold in *RPGRIP1L* KO, 2.6-fold in JBTS patient). BGJ-398 treatment
422 significantly reduced the number of EdU-incorporating cells in *RPGRIP1L* KO but not in JBTS
423 patient-derived organoids **(Supplementary Fig. 5A, B)**. Of note, similar results were obtained
424 whether considering the number of double $EdU^+/SOX2^+$ cells among the population of $SOX2^+$
425 cells, indicating more progenitors in S-phase **(Supplementary Fig. 5C).**
426 A chase assay was performed by removing EdU from the medium after 2 hours and fixing
427 organoids five days after the EdU pulse (i.e. day 23). The number of EdU label-retaining cells
428 was strongly reduced in both *RPGRIP1L* KO and JBTS patient conditions compared to controls
429 (~2-fold decrease) **(Fig. 7F, G)**. This indicates that, in the time-window analyzed (between day
430 18 and day 23), *RPGRIP1L* KO and JBTS patient-derived cells proliferated more than controls,
431 leading to the dilution of most EdU labeling. BGJ-398 treatment significantly restored the
432 number of label-retaining cells in both *RPGRIP1L* KO and JBTS patient-derived organoids **(Fig.
433 7F, G)**. EdU co-labeling with the progenitor marker SOX2 and the quantification of double
434 $EdU^+/SOX2^+$ cells among the $SOX2^+$ population showed similar results (**Fig. 7H**).
435 In addition, when dividing EdU+ cells into two categories—"strong" and "faint"—based on
436 labeling intensity, we observed that the "strong" EdU+ population, likely representing cells
437 that underwent at most one division after EdU incorporation, was the most affected in both
438 *RPGRIP1L*-deficient conditions and restored by BGJ-398 treatment **(Fig. 7I)**. Overall, FGF
439 overactivation in *RPGRIP1L*-deficient cerebellar organoids maintains SOX2+ progenitors in a
440 proliferative state and prevents their switch to neuronal differentiation and maturation,
441 reducing drastically Purkinje cell markers.
442
443 **DISCUSSION**
444
445 A crucial role of primary cilia for proper cerebellar development has been identified in mouse
446 mutants for ciliary genes, which present varying degrees of cerebellar hypoplasia [25,31–35].
447 However, the mechanisms linking mutations in ciliary genes to human cerebellar impairment,
448 as well as the developmental origin of specific JBTS patient cerebellar features, remain largely
449 unknown. Importantly, critical aspects of this disease may be missed in mouse models, as

450 cerebellar formation in humans presents unique features [9,10,64], and JBTS genes dysfunction
451 does not necessarily impact ciliogenesis the same way in both species [45]. To overcome this
452 issue, in this study we leveraged human cerebellar organoids to investigate the formation of
453 early cerebellar progenitors under healthy and pathological conditions linked to mutations in
454 *RPGRIP1L*, a JBTS causal gene. Our study uncovered an increased proliferation of neural
455 progenitors and a reduction of neurogenesis and Purkinje cell production in *RPGRIP1L*-
456 deficient cerebellar organoids. These defects are correlated with strong upregulation of
457 several FGF pathway related genes and increased levels of phosphorylated MEK1/2 pathway
458 effector at the cilium base. Rescue experiments by blocking FGF receptors (FGFRs)
459 demonstrate the causal link of FGF up-regulation to both neurogenesis-proliferation
460 imbalance and the reduction of Purkinje cell formation.
461
462 Given the important role of RPGRIP1L for ciliary functions, we analyzed cilia formation and
463 ciliary content in *RPGRIP1L*-deficient cerebellar organoids compared to controls. We showed
464 that the RPGRIP1L protein is differentially required for ciliogenesis in early neural progenitors,
465 since its loss causes severe ciliary defects in non-polarized progenitors, while mild
466 morphological defects are observed in polarized apical progenitors. This difference may result
467 from variations in ciliogenesis pathways and reinforces existing literature indicating a cell type-
468 specific requirement for RPGRIP1L at the ciliary transition zone. Indeed, studies in mice have
469 demonstrated that, in specific cell types, a compensatory mechanism involving the RPGRIP1L
470 paralogue – RPGRIP1 – could overcome RPGRIP1L depletion [52]. Moreover, in depth analysis of
471 cilia distribution and morphology in the mouse cerebral cortex and cerebellum challenged the
472 traditional view that cilia are uniformly present and identical in all brain regions and cell types
473 [65,66,28], a variability that may, at least partially, contribute to the differential vulnerability of
474 brain regions to mutations in ciliary genes. A reduced number of cilia on non-polarized cells
475 could either result from a direct effect of *RPGRIP1L* loss of function in cilia assembly or stability
476 [23,52] or from an indirect effect via FGF pathway deregulation. Indeed, FGF pathway activation
477 induces cilia lengthening in embryonic tissues and cell lines [67–69] while pathological sustained
478 FGF signalling induces shorter cilia [68]. In addition, a recent paper demonstrated the crucial
479 role of SP8 as a ciliogenesis inducer across embryonic cell types [70]. By performing FGF
480 signaling rescue experiments we found that BGJ-398 drug treatment neither improved nor
481 worsened cilia defects observed in *RPGRIP1L*-deficient conditions. This strongly suggests that

482 these ciliary alterations arise directly from *RPGRIP1L* loss of function, while dampening FGF
483 pathway restores the neurogenesis–proliferation balance downstream of cilia defects.
484
485 Our data suggest that defects in RPGRIP1L-deficient cerebellar organoids appear after the
486 initial cerebellum induction stages: while midbrain-hindbrain boundary markers were
487 expressed at day 7 in all genotype conditions, temporal expression analysis of typical
488 cerebellar cell markers revealed a strong reduction of all analyzed markers of the Purkinje
489 lineage, from day 21 to 35. Whether this reflects a defect in Purkinje cell specification and/or
490 in their differentiation remains to be determined. Purkinje cells being early-born neurons in
491 the human cerebellum (8-10 PCW) [8,9], the strong defect in their production in *RPGRIP1L*-
492 deficient organoids might stem from the general neurogenesis defect. Indeed, the concurrent
493 rescue of neurogenesis and expression of the Purkinje markers OLIG2, SKOR2 and CALB1
494 following FGFR inhibitor treatment strongly suggests that the two defects are linked. The GCP
495 population appears less affected when considering GCP marker RNA levels. However, we did
496 observe a 50% reduction in the number and staining intensity of BARHL1-expressing cells at
497 day 28, suggesting that the glutamatergic lineage might also be affected at later stages,
498 consistent with the late maturation of GNs in humans [9,48]. Transcriptome analysis also
499 revealed a severe downregulation of several integrins and ECM components, perturbing the
500 ECM-receptor system in *RPGRIP1L*-deficient organoids. Although the causes of this alteration
501 are unclear, it might participate in the neurogenesis and neuronal maturation impairment in
502 *RPGRIP1L*-deficient organoids. Indeed, the expression of ECM molecules is dynamically
503 regulated during brain development and plays prominent roles in neurogenesis, cell
504 migration, neurite outgrowth and synaptogenesis [71–73].
505
506 FGF8 is known as the key morphogen to establish early cerebellar territory *in vivo* [74]. Notably,
507 the dose, the precise location and the time window of FGF8 expression need to be tightly
508 controlled to allow proper cerebellar development [75]. Ectopically upregulating *Fgf8* in
509 cerebellar precursors increases their proliferation and overrides their normal program of cell
510 specification [76]. Moreover, conditional inactivation in the mouse isthmus of *Sprouty* genes
511 (*Spry1-2-4*), which are FGF direct targets acting as feedback loop negative regulators [77], results
512 in overactivation of FGF signaling and aberrant cerebellar development [78]. A growing literature
513 emphasizes the role of the FGF pathway in regulating the proliferative/neurogenic balance in

514 early neural development, by promoting progenitor proliferation at the expense of neuronal
515 differentiation during embryonic spinal cord elongation [79–81] and corticogenesis [82,83].
516 Interestingly, the development of the vermis in mice relies on a higher and longer FGF8 dosage
517 than the hemispheres [75,84]. During early developmental stages, the region expressing FGF8
518 corresponds to the prospective vermis [85], which has been identified as a direct derivative of
519 these FGF8-expressing isthmic cells [86].
520 In our cerebellar differentiation protocol, control organoids downregulated *FGF8* after day 7,
521 while *RPGRIP1L*-deficient organoids displayed a massive FGF8 up-regulation from day 14 to
522 21. Consistent with current literature, we showed that the increased levels of FGF ligands
523 (*FGF8, FGF17, FGF19*) and pathway activation, as indicated by the expression of *ETV*4-5 target
524 genes, were responsible for the impaired neurogenesis and neuronal differentiation observed
525 upon *RPGRIP1L* depletion.
526 We thus addressed the mechanisms that could underlie FGF upregulation upon *RPGRIP1L*-
527 deficiency. A recent paper showed that, in mouse embryos and in cell culture, FGF receptors
528 1 and 2 localize to the cilium, and that downstream activated MAPK effectors are present at
529 the cilium base. We found that in our cerebellar organoids, the activated form of the MAPK
530 kinase MEK1/2 localized almost exclusively to the cilium base in most cells, except in mitotic
531 cells where it is at the spindle poles. In RPGRIP1L-deficient organoids, activated MEK1/2 still
532 localized to the basal body, even in cells with no visible cilia. Moreover, the amount of
533 pMEK1/2 at cilia was increased. Thus, our data show that 1) FGF signaling is activated at the
534 cilium base in cerebellar progenitors, 2) RPGRIP1L and cilia are not required for FGF signaling
535 activation in these cells, nor for MEK1/2 recruitment adjacent to basal bodies and 3) on the
536 contrary, RPGRIP1L deficiency leads to a defect in signal attenuation.
537 In which cell types is FGF signaling active? We revealed the presence of FGF8 protein mainly
538 in apical neural progenitors, suggesting that they are the FGF8 producing cells. In terms of
539 responding cells, both apical and non-apical neural progenitors activate the pathway, as seen
540 with activated MEK1/2 and SP8 levels. We thus propose that the FGF pathway activation at
541 the cilium base initiates a positive loop by increasing the number of proliferating progenitors
542 that themselves activate the FGF pathway. We provide evidence that, once engaged, this
543 mechanism could be self-sustaining. We propose that the SP8 transcription factor, a well-
544 known inducer and target of FGF8 [87,88,59], participates in this self-amplification loop, being

545 significantly upregulated at both day 14 and 21 (see DEGs tables) and expressed by an
546 increased number of cells in all *RPGRIP1L*-deficient conditions.
547
548 An essential question raised by our study is the link between the early increased proliferation
549 observed in cerebellar organoids and the vermis hypoplasia found in JBTS patients. Although
550 we cannot exclude that the context of organoids could favor specific manifestations of the
551 *RPGRIP1L* mutant phenotype that are not revealed *in vivo*, several hypotheses could explain
552 these apparently opposite phenotypes. First, an early over-proliferation could trigger later cell
553 death, as observed upon loss of function of the kinase DYRK1A [89]. Alternatively, an increase in
554 early progenitor numbers could preferentially populate the cerebellar hemispheres at the
555 expense of the vermis. Indeed, lineage studies in mice highlight different medio-lateral
556 distribution of cerebellar VZ clones according to their birth dates [90,91]. Finally, an expansion of
557 the midbrain-hindbrain boundary signaling center due to FGF8 overexpression could impair
558 morphogenetic movements leading to midline fusion of the bilateral cerebellar primordia and
559 thus vermis formation, as shown in chicken embryos [92]. The long-term consequences of
560 impaired differentiation and sustained proliferation in cerebellar organoids will have to be
561 investigated.
562 Whatever the mechanism, increased proliferation in cerebellar organoids is consistent with
563 data obtained in mouse mutants for two JBTS causal genes, KIF17 [93] and SUFU. The case of
564 SUFU, a negative regulator of the HH pathway that acts at the cilium, is particularly striking.
565 In mice, conditional invalidation of SUFU in GCPs or Purkinje progenitors leads to protracted
566 proliferation and delayed differentiation, as well as to FGF8 pathway upregulation in cerebellar
567 progenitors [94–96]. Notably, early SUFU invalidation in the cerebellar anlage leads to loss of the
568 vermis [95], mimicking a ciliopathy phenotype. In humans, germline SUFU haploinsufficiency or
569 recessive hypomorphic mutations in SUFU can be associated with mild forms of JBTS
570 encompassing cerebellar vermis hypoplasia [97,98]. On the other hand, germline SUFU
571 haploinsufficiency is also a strong risk factor for the development of severe infantile
572 medulloblastoma (of SHH-MB class) [99,100]. Additionally, some SUFU variants have been
573 reported both in JBTS and cancer [98]. This, together with our data on *RPGRIP1L* deficiency in
574 cerebellar organoids, raises the puzzling question of potential common mechanisms between
575 early cerebellar progenitor hyperproliferation and later vermis hypoplasia.
576

577 The relevance of our study for JBTS pathology is emphasized by the similar phenotypes of
578 *RPGRIP1L* KO organoids with organoids derived from a JBTS patient's iPSC line. The JBTS
579 patient donor of the NG2266 cell line used in this study, exhibits a very severe neurological
580 phenotype, correlated with vermis hypoplasia and partial aplasia, as revealed by encephalic
581 magnetic resonance imaging (MRI). The patient carries two biallelic heterozygous mutations
582 in the *RPGRIP1L* gene: a nonsense mutation at the end of the first C2 protein domain, and a
583 splice variant that results in the generation of a stop codon at the beginning of the second C2
584 domain. Given the importance of both C2 domains for RPGRIP1L function [101,102,25,103,21], a stop
585 codon in these domains is likely to impair protein functionality. Indeed, similar to the
586 *RPGRIP1L* KO condition, JBTS patient (NG2266)-derived organoids lacked RPGRIP1L protein at
587 the ciliary transition zone. This further underscores the strong phenotypical similarity
588 observed between *RPGRIP1L* KO and JBTS patient (NG2266)-derived organoids. Furthermore,
589 targeted pharmacological inhibition of FGFR using BGJ-398/Infigratinib, an FDA-approved drug
590 currently used in oncology and to treat hypochondroplasia [63], is sufficient to rescue the
591 proliferative-neurogenic balance and to restore Purkinje cell lineage formation, both in
592 *RPGRIP1L* knockout hiPSC lines and in the Joubert syndrome patient line, establishing a
593 mechanistic link between FGF overactivation and the observed phenotypical alterations.
594
595 More generally, it will be crucial to determine whether the molecular alterations reported in
596 this study have broader relevance by also occurring in cerebellar organoids with mutations in
597 other JBTS genes, or if they are specific to *RPGRIP1L* depletion. Indeed, not all JBTS patients
598 present cerebellar vermis hypoplasia; in milder cases, the cerebellar vermis may be dysplastic
599 without a reduction in size [104]. It will be particularly helpful to investigate whether FGF
600 signaling could be specifically disrupted in cerebellar organoids from patients with severe
601 vermis hypoplasia, as it might be of predictive value for the severity of the neurological
602 phenotype.
603
604 In conclusion, with this work we provide an example of a cerebellar organoid approach to
605 investigate potential pathogenetic mechanisms underlying a human disease. Our results
606 uncover neurogenesis defects driven by increased FGF signaling, thereby offering a novel
607 framework for investigating the etiology of cerebellar defects in JBTS and other
608 neurodevelopmental diseases. We further highlight that RPGRIP1L ciliary protein performs

609 complex rheostat functions in signaling, revealing its crucial role for proper FGF signal
610 attenuation in human neural progenitors, while in other cellular contexts in mice, Rpgrip1l is
611 necessary to reach the highest level of Hedgehog activation [24].
612
613
614 **MATERIAL AND METHODS**
615
616 **Ethics**
617 The work performed in this manuscript complies with all relevant ethical regulations. The
618 obtaining and manipulation of human iPSC lines were performed under ethical agreements
619 from the French Ministry of Higher Education and Research DC-2025-7003 (for the UCSFi001-
620 A and PCIi033-A lines, control and RPGRIP1L-KO) and DC-2025-7496 (for the JBTS patient line)
621 and under GMO authorization number DUO-9509.
622
623 **hiPSC culture**
624 hiPSCs were thawed in mTeSR+ medium (Stem Cell Technologies #100-0276) in the presence
625 of Rock-inhibitor Y-27632 (5µM, Stemgent-Ozyme #04-0012) and cultured on Matrigel
626 (Corning, VWR #354277) coated plates under standard conditions at 37°C upon confluency of
627 70-80%. The medium was changed every two days. Passaging was performed using ReLeSR
628 (Stem Cell Technologies #05872) and testing for potential mycoplasma contamination was
629 performed regularly by Eurofins genomic (Mycoplasmacheck). Accutase (Stem Cell
630 Technologies #07920) was used for the dissociation of hiPSC colonies into single cells prior to
631 the differentiation protocol.
632
633 **Clinical features of the patient COR201 and characterization of the mutant Identification of**
634 **the RPGRIP1L RNA products derived from the NG2266 hiPSC c.2304+1G>T splice variant**
635 **allele.**
636 The NG2266 cell line is derived from the male patient COR201 [50] who was last examined at
637 the age of 17. He presented a molar tooth sign on brain MRI and his neurological examination
638 revealed hypotonia, psychomotor delay, neonatal breathing dysregulation, ocular-motor
639 apraxia, nystagmus and severe intellectual disability. Post-axial polydactyly of the left hand
640 was present at birth. During evolution, he suffered severe visual impairment and strabismus,

641 severe renal dysfunction (chronic renal failure at the age of 11, which required renal
642 transplantation at age 14), as well as chronic liver disease.
643 We demonstrated by sequencing PCR products from NG2266 hiPSCs cDNA that the splice
644 variant c.2304+1G>T resulted in intron retention leading to an early stop codon at position
645 788 (S788X). Primer 1 (Forward: GTATCCATAAACTAGAAGCCCAAT) was designed at the junction
646 between exon 14 and 15; primer 2 (Reverse: GGGTTAAGGTTACAGGGGATCTC) was placed in
647 the intron between exon 16 and 17; Primer 3 (Reverse: AATATTCCTGAGATACACCTGTC) was
648 positioned at the junction between exon 17 and 18 **(Supplementary Fig. 6A)**. PCR products
649 were analyzed on agarose gel and showed that primer pair 1-2 amplified an 813 bp region in
650 the cDNA derived from JBTS patient (NG2266) hiPSCs but not from the control condition
651 **(Supplementary Fig. 6B)**. Primer pair 1-3 amplified a 1009 bp region, both in the control and
652 in JBTS patient cDNA. As expected, NG2266 second allele (c.2050C>T/p.Q684X) presents a
653 nonsense mutation that does not affect the cDNA structure, resulting in a PCR product of the
654 same size as control alleles. On the contrary, using the primer pair 1-3, the c.2304+1G>T allele
655 could not be amplified from cDNA given that intron retention would give rise to a 3969 bp PCR
656 product **(Supplementary Fig. 5B')**.
657 Primer pair 1-2 PCR product from NG2266 hiPSCs was sequenced to confirm the intron
658 retention. An ATG stop codon appears 29 nt after the beginning of the intron sequence, most
659 likely giving rise to a truncated form of the protein **(Supplementary Fig. 6C)**.
660 Moreover, an additional mutation was identified in the exon 16: c.2231 G>A (p. R744Q).
661
662 **Differentiation of hiPSCs into cerebellar organoids**
663 After two amplification passages, hiPSC lines (characterized in [50,52]) were dissociated into
664 single cells using Accutase (Stem Cell Technologies #07920) and resuspended in mTeSR+
665 medium supplemented with 10 µM ROCK inhibitor. Then, cells were promptly re-aggregated
666 using AggreWell™800 microwell plates (StemCell Technologies) following the manufacturer's
667 instructions. Cells were seeded at a density of 1.8 × 10^6 cells per well (6,000 cells per
668 microwell). This corresponded to day 0 of the cerebellar differentiation protocol. Two days
669 later the entire medium was replaced with the chemically defined medium (gfCDM), slightly
670 modified compared to [37], consisting of vol:vol Isocove's modified Dulbecco's medium (Thermo
671 Fisher #12440053)/Advanced DMEM/F-12 (Thermo Fisher #12634028), chemically defined
672 lipid concentrate (1% v/v, Thermo Fisher #11905031), monothioglycerol (450 µM, Sigma

673 #M6154), apo-transferrin (15 µg/ml, Sigma #T1147), crystallization-purified BSA (5 mg/ml,
674 >99%, Sigma #5470), and 50 U/ml penicillin/50 µg/ml streptomycin (P/S, Thermo Fisher
675 #15140122). The medium was also supplemented with insulin (7 µg/ml, Sigma #I9278) and
676 used from day 2 to day 21. Different factors were added to the medium at different timepoints
677 as represented in Fig. 1A. Recombinant human basic FGF (FGF2, 50 ng/ml, PeproTech # 100-
678 18B) and SB431542 (SB, 10 µM, Stemgent-Ozyme #04-0010) were added to the culture on day
679 2. On day 4, floating aggregates were transferred from microwell plates to ultra-low
680 attachment dishes (Corning #3261) and total medium change with drug refreshment was
681 performed. On day 7 embryoid bodies(EBs)-containing dishes were transferred to an orbital
682 shaker (3 mm orbit, Thermo Scientific #88881102B) and maintained under orbital agitation of
683 100 rpm until the end of the protocol. Total medium change with 2/3 of the initial amount of
684 FGF2 and SB431542 was performed on day 7, day 9 and day 11. On day 14, FGF2 and SB431542
685 were replaced by medium change supplemented with recombinant FGF19 (100 ng/ml;
686 PeproTech #100-32). The same medium change was also performed at day 16 and 18. From
687 day 21 onward, the aggregates were cultured in Neurobasal medium (Thermo Fisher
688 #21103049) supplemented with GlutaMax I (Thermo Fisher #35050061), N2 supplement
689 (Thermo Fisher #17502048), and P/S 1% (Thermo Fisher #15140122). Total medium changes
690 were performed on day 23, 25, 28, 30 and 32. Recombinant human SDF1 (300 ng/ml,
691 PeproTech #300-28A) was added to the culture from day 28 onward (**Fig. 1A**).
692 For pan-FGFR inhibition, BGJ-398/Infigratinib [63] was first added at day 11 at a concentration
693 of 100 nM and renewed on days 14 and 16. At day 18 total medium was replaced by fresh
694 medium devoid of BGJ-398.
695
696 **EdU treatment and labeling**
697 Cerebellar organoids at day 18 were incubated using 10 µM EdU (Click-iT EdU Imaging Kit,
698 Invitrogen) dissolved in growth medium for 2 h at 37 °C and then washed twice with PBS.
699 Around 30 organoids per genotype were collected and fixed for 20 minutes at room
700 temperature in 4% cold PFA. The remaining organoids, around 30 per genotype, were kept in
701 culture after washing for a 5-day chase until day 23 of the differentiation protocol, when they
702 were collected and fixed in the same way.
703 Fixed organoids were embedded in OCT following the procedure described in the section
704 Organoids embedding and Cryosectioning**.** EdU labeling detection on cryosections was

705 performed according to the Click-iT EdU Imaging Kit manufacturer's instruction at the end of
706 our immunostaining protocol (refer to the following section "Immunofluorescence").
707
708 **Organoid Size Analysis**
709 To monitor the organoid size, bright-field images were acquired at different time-points (every
710 seven days). Organoid area was calculated by manually dragging a line with the freehand
711 selections tool on Fiji (ImageJ; National Institutes of Health) and subsequently measuring the
712 object area. Organoid area was measured in several independent experiments (N=3 Ph2 line,
713 N=3 Wtc11 line, N=3 NG2266 line), n=10-60 organoids were analyzed per experiment per
714 condition. Results are presented as the mean ± SEM of organoid averages from each individual
715 experiment.
716
717 **Organoids embedding and Cryosectioning**
718 Organoids were collected every seven days during differentiation from day 7 to 35, rinsed with
719 PBS and fixed in cold PFA (4 %) for 20 min at 4 °C. Then organoids were rinsed in PBS and
720 incubated in 30 % sucrose in PBS until completely saturated. Cryoprotected organoids were
721 embedded in OCT matrix (Cell Path #KMA-0100-00A) in plastic molds and stored at -80 °C. 12
722 µM cryostat sections were prepared and stored at -20 °C.
723
724
725 **Immunofluorescence**
726 Cryostat sections of organoids were washed in PBS/0.1% Triton X-100. An optional step of
727 antigen-retrieval with Citrate-Buffer was performed only for cilia staining (INPP5E and
728 Gamma-TUBULIN antibodies). After washing, cryosections were incubated with a blocking
729 solution containing 10% NGS in PBS/0.1% Triton-X100 for at least 2 hours. The sections were
730 incubated overnight at 4 °C with primary antibodies **(Supplementary Table 5)** diluted in a
731 solution containing 1% NGS in PBS/0.1% Triton-X100. Next day, the slides were washed 3 x 10
732 min with PBS/0.1% Triton-X100 and incubated with secondary antibodies at 1:400 dilution
733 **(Supplementary Table 6)** and DAPI (Merck #1.24653) in 1% NGS/PBS/0.1 % Triton X-100 for 2
734 hours. After final washing steps with PBS/0.1 %Triton X-100 for at least 1 hour, sections were
735 mounted with Mowiol (Roth #0713.2).
736

737 **Image acquisition**

738 Fluorescence image acquisition of cerebellar progenitors and neuronal markers was
739 performed at room temperature using a Zeiss Observer Z1 equipped with an Apotome
740 module, an Axiocam 506 monochrome cooled CCD camera and a 20x objective. Z-stacks with
741 1 µM step were acquired. All images were processed with Zen software (blue edition).

742 For cilia analyses, Z-stacks images with 250 nM steps were acquired using a confocal
743 microscope (LSM 980 upright, Carl Zeiss AG) and a 63x oil objective with a NA 1.4. Phospho-
744 MEK1/2 images used for quantification were acquired as Z-stacks with 250 nM steps with
745 LSM980 confocal microscope using a 63x oil objective with a NA 1.4 and a zoom of 2. All
746 confocal images were acquired using a monochrome charge-coupled device camera and
747 processed with Zen software (black edition).

748 For Super-resolution imaging of the pMEK1/2 signal, the LSM980 Airyscan confocal (Zeiss) was
749 used in SR mode and image stacks were acquired every 20 nM with a 63x objective and a zoom
750 value of 3.

751

752 **Quantification of immunofluorescent staining and statistical analyses**

753 The number of positive cells in immunofluorescence staining was quantified on 7µm Z-
754 projections using the Cellpose environment
755 (https://cellpose.readthedocs.io/en/latest/installation.html) for cell segmentation. Each
756 image was segmented using the DAPI channel to generate a mask identifying all nuclei. The
757 intensity of the target channel was then measured for each nucleus by uploading the MAX-
758 projection image and the corresponding ROI mask (generated with Cellpose) into Fiji (ImageJ;
759 National Institutes of Health). Mean intensity was calculated for each ROI, and a threshold
760 was applied to distinguish marker-positive cells from background immunostaining. Only cells
761 above this threshold were counted, and the ratio to the total number of nuclei (ROIs in the
762 mask) was determined. Nuclei smaller than 10 µm² were excluded, as they were considered
763 pycnotic cells.

764 For quantitative analyses of ZO1 staining at the apical side of the cells, positive areas were
765 defined and measured by manually setting common thresholds in Fiji for all genotypes. For
766 each image, the DAPI positive area was also determined and measured by manually setting
767 thresholds. The percentage of ZO1 positive area per organoid slice was determined after
768 dividing the ZO1 calculated area by the DAPI area.

769 Analysis of ciliary density was performed by manually counting the number of cilia axonemes
770 (INPP5E staining) over the number of basal bodies (Gamma-Tubulin staining). Measurements
771 of axonemal INPP5E intensity and ciliary length were performed on unprocessed images (raw
772 data) using the segmented line tool on Fiji to draw ROIs corresponding to each cilium. Mean
773 gray value and length were then extracted for each ROI of an image. INPP5E mean intensity is
774 calculated by subtracting the mean background value of an image to the mean gray value of
775 each ROI in the image. Data are represented as "relative mean intensity" by setting the mean
776 value of all control cilia (ROIs) at 1. After quantifications were performed, representative
777 images were processed by means of background subtraction and contrast settings via Fiji.
778 pMEK1/2 quantifications were performed on Z-stacks (7.5µ thickness), tracing ROI manually
779 at the base of each cilium between the basal body stained with GAMMA-TUBULIN and the
780 axoneme labelled by ARL13B. The mean intensity of each ROI was measured using FIJI
781 software, after removing a background value. For each field of 67.3µm X 67.3µm, 20 to 100
782 ROIs were measured and the mean value for each field was plotted.
783 All data are presented as mean ± SEM. One-Way ANOVA Kruskal-Wallis and Dunn's test or
784 Welch's t test were performed as indicated in the figure legends and the following statistical
785 significances were considered: *P<0.033, **P<0.0021, ***P<0.0002 and ****P<0.0001. All
786 statistical data analysis and graph illustrations were performed using GraphPad Prism
787 (GraphPad Software).
788
789 **Total RNA isolation and qPCR analyses**
790 Control, *RPGRIP1L* KO and JBTS patient-derived cerebellar organoids from different hiPSCs
791 lines (Ph2, Wtc11, NG2266) and several independent experiments were collected every seven
792 days from day 7 to 35 of the differentiation protocol and washed with PBS. RNA was isolated
793 using the RNeasy Kit (Qiagen #74104) and RNAse-free DNase Set (Qiagen #79254) following
794 manufacturer's instructions. 1µg of isolated RNA was retro-transcribed into cDNA using the
795 GoScript Reverse Transcriptase Kit (Promega #A5001). For quantitative real-time PCR, a cDNA
796 dilution (equal to 15 ng of starting RNA per well) was used in a Maxima SYBR Green/ROX qPCR
797 Master Mix 2x (Thermo Scientific #K0222). Duplicate reactions for each sample were prepared
798 and the samples were run in a Step One Real-Time PCR System Thermal Cycling Block (Applied
799 Biosystems #4376357). GAPDH housekeeping gene was used as reference. Primer pairs are
800 listed in **Supplementary Table 7.** The analysis of real-time data was performed using the

801 included StepOne Software version 2.0 and graphs were generated using GraphPad Prism
802 (GraphPad Software).
803
804 **Total RNA isolation and Bulk RNAseq analysis on cerebellar organoids**
805 RNA was isolated as described above using the RNeasy Kit (Qiagen #74104) and RNAse-free
806 DNase Set (Qiagen #79254) from control, *RPGRIP1L* KO and JBTS patient-derived cerebellar
807 organoids at different timepoint and from several independent experiments (see
808 Supplementary Tables 2-4 for sample details and N). RNA quality was determined by
809 measuring the RNA integrity number (RIN) via the High Sensitive RNA Screen Tape Analysis kit
810 (Agilent Technologies #5067) on the TapeStation system (Agilent Technologies). A RIN above
811 9.5 was considered as good quality RNA and 250 ng RNA in a total volume of 25 µl was
812 prepared per sample for further procedure. Bulk RNAseq was realized by the Genotyping and
813 Sequencing Core Facility of the Paris Brain Institute (iGenSeq, ICM Paris). Poly A stranded cDNA
814 libraries were built with the kit "Illumina® Stranded mRNA Prep" and their quality checked on
815 "AGILENT Tapestation 2100". 125 ng of each library was sequenced on both strands to produce
816 between 33-44 Millions reads (100 bases long) using a Novaseq6000 ILLUMINA.
817 RNAseq data processing was performed in Galaxy under supervision of the ARTBio platform
818 (IBPS, Paris). Paired-end RNA reads were aligned against the homo sapiens hg38 genome by
819 using the STAR aligner (v2.7.10, Galaxy wrapper v4) [105] and the gene annotations gtf files
820 GRCh38.109. Quality of sequencing was controlled with fastQC (Galaxy wrapper
821 v0.74+galaxy0) and MultiQC (Galaxy wrapper v1.11+galaxy1) [106]. Gene expression was
822 assessed by counting sequencing reads aligned to gene exons with featureCounts (Galaxy
823 wrapper v2.0.3+galaxy2) [107]. Raw counts were further converted to normalized gene
824 expression values using the log2(tpm+1) transformation where tpm is the count of transcript
825 aligned reads per length of transcript (kb) per million of total mapped reads (Galaxy tool
826 "cpm_tpm_rpk" v0.5.2) and heatmap visualizations were produced with the Galaxy tool
827 "high_dim_heatmap" (v3.1.3+galaxy0) using the normalized gene expression values.
828 Differentially expressed genes (DEGs) were selected from the gene raw read counts using
829 DESeq2 (Galaxy wrapper v2.11.40.8+galaxy0) [108] and the Benjamini-Hochberg p-adjusted
830 cutoff 0.05. DESeq2 statistical tables were used for generation of Volcano Plots (Galaxy tool id
831 "volcanoplot" v0.0.5) [109] and for the analysis of overrepresented gene ontology (GO)
832 categories (Metascape software, https://metascape.org/gp/index.html#/main/step1) [110].

ACKNOWLEDGEMENTS

We particularly thank Chloé Chaumeton and France Lam from the IBPS imaging platform I2PS for their help on image acquisition. We thank the IBPS Bioinformatics facility of which C.A. is a former member. We thank the iGenSeq sequencing platform at the ICM for reliable and fast processing of our samples. We are very grateful to Stéphane Nedelec for providing advice on BGJ-398/Infigratinib drug usage in hiPSCs and to Aline Stedman for scientific discussions and advice on manuscript organization. We thank Alexis Eschstruth for his kind contribution to the PCR analysis to identify the cDNA product of JBTS patient c.2304+1G>T splice variant. This work was supported by funding to SSM from the *Fondation pour la Recherche Médicale (“Equipe FRM”* projects EQU201903007943 and EQU202503020010), from the *Fondation pour la Recherche sur le Cancer* (ARCPJA2024080008603), from the *Agence Nationale de la Recherche* - ERA-NET Neuron 2021 “NDCil” (ANR-21-NEU2-0009-03) project and PRC AAPG2024 “CiCerO” project, from the *Fondation Maladies Rares* and the *Association Mieux vivre avec le syndrome de Joubert* under the reference “ASSOJoubert_2024_Schneider”. L.B.’s PhD was funded by Sorbonne Université (Doctoral school *Complexité du Vivant* ED515). A.W. received funding from the German Research Foundation (DFG; WI 5451/1-1). Work in E.M.V.’s lab was supported by Italian Ministry of Health - ERA-NET Neuron 2021 “NDCil” (ERP-2021-23680733).

BIBLIOGRAPHY

1. Stoodley, C. J. The Cerebellum and Neurodevelopmental Disorders. *The Cerebellum* **15**, 34–37 (2016).
2. Leto, K. *et al.* Consensus Paper: Cerebellar Development. *The Cerebellum* **15**, 789–828 (2016).
3. Crossley, P. H., Martinez, S. & Martin, G. R. Midbrain development induced by FGF8 in the chick embryo. *Nature* **380**, 66–68 (1996).
4. Chi, C. L., Martinez, S., Wurst, W. & Martin, G. R. The isthmic organizer signal FGF8 is required for cell survival in the prospective midbrain and cerebellum. *Development* **130**, 2633–2644 (2003).
5. Hoshino, M. *et al.* Ptf1a, a bHLH Transcriptional Gene, Defines GABAergic Neuronal Fates in Cerebellum. *Neuron* **47**, 201–213 (2005).
6. Ben-Arie, N. *et al.* Math1 is essential for genesis of cerebellar granule neurons. *Nature* **390**, 169–172 (1997).

7. Machold, R. & Fishell, G. Math1 Is Expressed in Temporally Discrete Pools of Cerebellar Rhombic-Lip Neural Progenitors. *Neuron* **48**, 17–24 (2005).
8. Rakic, P. & Sidman, R. L. Histogenesis of cortical layers in human cerebellum, particularly the lamina dissecans. *J. Comp. Neurol.* **139**, 473–500 (1970).
9. Aldinger, K. A. *et al.* Spatial and cell type transcriptional landscape of human cerebellar development. *Nat. Neurosci.* **24**, 1163–1175 (2021).
10. Haldipur, P. *et al.* Spatiotemporal expansion of primary progenitor zones in the developing human cerebellum. *Science* **366**, 454–460 (2019).
11. Sillitoe, R. V. & Joyner, A. L. Morphology, Molecular Codes, and Circuitry Produce the Three-Dimensional Complexity of the Cerebellum. *Annu. Rev. Cell Dev. Biol.* **23**, 549–577 (2007).
12. Maria, B. L. *et al.* 'Joubert Syndrome' Revisited: Key Ocular Motor Signs With Magnetic Resonance Imaging Correlation. *J. Child Neurol.* **12**, 423–430 (1997).
13. Bachmann-Gagescu, R. *et al.* Healthcare recommendations for Joubert syndrome. *Am. J. Med. Genet. A.* **182**, 229–249 (2020).
14. Bachmann-Gagescu, R. *et al.* Joubert syndrome: a model for untangling recessive disorders with extreme genetic heterogeneity. *J. Med. Genet.* **52**, 514–522 (2015).
15. Serpieri, V. *et al.* Recurrent, founder and hypomorphic variants contribute to the genetic landscape of Joubert syndrome. *J. Med. Genet.* **60**, 885–893 (2023).
16. Mitchison, H. M. & Valente, E. M. Motile and non-motile cilia in human pathology: from function to phenotypes: Motile and non-motile ciliopathies. *J. Pathol.* **241**, 294–309 (2017).
17. Reiter, J. F. & Leroux, M. R. Genes and molecular pathways underpinning ciliopathies. *Nat. Rev. Mol. Cell Biol.* **18**, 533–547 (2017).
18. Mill, P., Christensen, S. T. & Pedersen, L. B. Primary cilia as dynamic and diverse signalling hubs in development and disease. *Nat. Rev. Genet.* **24**, 421–441 (2023).
19. Goetz, S. C. & Anderson, K. V. The primary cilium: a signalling centre during vertebrate development. *Nat. Rev. Genet.* **11**, 331–344 (2010).
20. Reiter, J. F., Blacque, O. E. & Leroux, M. R. The base of the cilium: roles for transition fibres and the transition zone in ciliary formation, maintenance and compartmentalization. *EMBO Rep.* **13**, 608–618 (2012).
21. Jensen, V. L. *et al.* Formation of the transition zone by Mks5/Rpgrip1L establishes a ciliary zone of exclusion (CIZE) that compartmentalises ciliary signalling proteins and controls PIP_2 ciliary abundance. *EMBO J.* **34**, 2537–2556 (2015).
22. Wiegering, A. *et al.* Rpgrip1l controls ciliary gating by ensuring the proper amount of Cep290 at the vertebrate transition zone. *Mol. Biol. Cell* **32**, 675–689 (2021).
23. Besse, L. *et al.* Primary cilia control telencephalic patterning and morphogenesis via Gli3 proteolytic processing. *Development* **138**, 2079–2088 (2011).
24. Andreu-Cervera, A. *et al.* The ciliopathy gene *ftm/rpgrip1l* controls mouse forebrain patterning via region-specific modulation of hedgehog/gli signaling. *J. Neurosci.* 2199–18 (2019) doi:10.1523/JNEUROSCI.2199-18.2019.
25. Delous, M. *et al.* The ciliary gene RPGRIP1L is mutated in cerebello-oculo-renal syndrome (Joubert syndrome type B) and Meckel syndrome. *Nat. Genet.* **39**, 875–881 (2007).
26. Chang, C.-H. *et al.* Atoh1 Controls Primary Cilia Formation to Allow for SHH-Triggered Granule Neuron Progenitor Proliferation. *Dev. Cell* **48**, 184-199.e5 (2019).

27. Ong, T., Trivedi, N., Wakefield, R., Frase, S. & Solecki, D. J. Siah2 integrates mitogenic and extracellular matrix signals linking neuronal progenitor ciliogenesis with germinal zone occupancy. *Nat. Commun.* **11**, 5312 (2020).
28. Ott, C. M. *et al.* Permanent deconstruction of intracellular primary cilia in differentiating granule cell neurons. *J. Cell Biol.* **223**, e202404038 (2024).
29. Chizhikov, V. V. *et al.* Cilia Proteins Control Cerebellar Morphogenesis by Promoting Expansion of the Granule Progenitor Pool. *J. Neurosci.* **27**, 9780–9789 (2007).
30. Spassky, N. *et al.* Primary cilia are required for cerebellar development and Shh-dependent expansion of progenitor pool. *Dev. Biol.* **317**, 246–259 (2008).
31. Lancaster, M. A. *et al.* Defective Wnt-dependent cerebellar midline fusion in a mouse model of Joubert syndrome. *Nat. Med.* **17**, 726–731 (2011).
32. Abdelhamed, Z. A. *et al.* The ciliary Frizzled-like receptor Tmem67 regulates canonical Wnt/β-catenin signalling in the developing cerebellum via Hoxb5. *Sci. Rep.* **9**, 5446 (2019).
33. Damerla, R. R. *et al.* Novel Jbts17 mutant mouse model of Joubert syndrome with cilia transition zone defects and cerebellar and other ciliopathy related anomalies. *Hum. Mol. Genet.* **24**, 3994–4005 (2015).
34. Bashford, A. L. & Subramanian, V. Mice with a conditional deletion of *Talpid3* (*KIAA0586*) – a model for Joubert syndrome. *J. Pathol.* **248**, 396–408 (2019).
35. Suciu, S. K., Long, A. B. & Caspary, T. Smoothened and ARL13B are critical in mouse for superior cerebellar peduncle targeting. *Genetics* **218**, iyab084 (2021).
36. Aguilar, A. *et al.* Analysis of human samples reveals impaired SHH-dependent cerebellar development in Joubert syndrome/Meckel syndrome. *Proc. Natl. Acad. Sci.* **109**, 16951–16956 (2012).
37. Muguruma, K., Nishiyama, A., Kawakami, H., Hashimoto, K. & Sasai, Y. Self-Organization of Polarized Cerebellar Tissue in 3D Culture of Human Pluripotent Stem Cells. *Cell Rep.* **10**, 537–550 (2015).
38. Nayler, S. P. & Becker, E. B. E. The Use of Stem Cell-Derived Neurons for Understanding Development and Disease of the Cerebellum. *Front. Neurosci.* **Volume 12-2018**, (2018).
39. Silva, T. P. *et al.* Maturation of Human Pluripotent Stem Cell-Derived Cerebellar Neurons in the Absence of Co-culture. *Front. Bioeng. Biotechnol.* **8**, 70 (2020).
40. Atamian, A. *et al.* Human cerebellar organoids with functional Purkinje cells. *Cell Stem Cell* **31**, 39-51.e6 (2024).
41. Kagermeier, T. *et al.* Human organoid model of pontocerebellar hypoplasia 2a recapitulates brain region-specific size differences. (2024).
42. Guerra, M., Medici, V., La Sala, G. & Farini, D. Unravelling the Cerebellar Involvement in Autism Spectrum Disorders: Insights into Genetic Mechanisms and Developmental Pathways. *Cells* **13**, (2024).
43. Ryu, S. *et al.* Modeling Friedreich's ataxia with Bergmann glia-enriched human cerebellar organoids. *bioRxiv* 2025.05.16.654315 (2025) doi:10.1101/2025.05.16.654315.
44. Aprile, D. *et al.* Benchmarking cerebellar organoids to model autism spectrum disorder and human brain evolution. *bioRxiv* 2025.05.14.653684 (2025) doi:10.1101/2025.05.14.653684.
45. Wiegering, A. *et al.* A differential requirement for ciliary transition zone proteins in human and mouse neural progenitor fate specification. *Nat. Commun.* **16**, 3258 (2025).
46. Andreu-Cervera, A., Catala, M. & Schneider-Maunoury, S. Cilia, ciliopathies and hedgehog-related forebrain developmental disorders. *Neurobiol. Dis.* **150**, 105236 (2021).

47. Silva, T. P. *et al.* Transcriptome profiling of human pluripotent stem cell-derived cerebellar organoids reveals faster commitment under dynamic conditions. *Biotechnol. Bioeng.* **118**, 2781–2803 (2021).
48. Li, M. *et al.* Integrative functional genomic analysis of human brain development and neuropsychiatric risks. *Science* **362**, eaat7615 (2018).
49. Wechsler-Reya, R. J. & Scott, M. P. Control of Neuronal Precursor Proliferation in the Cerebellum by Sonic Hedgehog. *Neuron* **22**, 103–114 (1999).
50. Pollara, L. *et al.* Production and characterisation of four Joubert syndrome patient-derived induced pluripotent stem cell (iPSC) lines with mutations in either RPGRIP1L or CPLANE1 genes. *Stem Cell Res.* **86**, 103734 (2025).
51. Richards, S. *et al.* Standards and guidelines for the interpretation of sequence variants: a joint consensus recommendation of the American College of Medical Genetics and Genomics and the Association for Molecular Pathology. *Genet. Med.* **17**, 405–424 (2015).
52. Wiegering, A. *et al.* Cell type-specific regulation of ciliary transition zone assembly in vertebrates. *EMBO J.* **37**, (2018).
53. Taverna, E. & Huttner, W. B. Neural Progenitor Nuclei IN Motion. *Neuron* **67**, 906–914 (2010).
54. Das, R. M. & Storey, K. G. Apical Abscission Alters Cell Polarity and Dismantles the Primary Cilium During Neurogenesis. *Science* **343**, 200–204 (2014).
55. Laguesse, S., Peyre, E. & Nguyen, L. Progenitor genealogy in the developing cerebral cortex. *Cell Tissue Res.* **359**, 17–32 (2015).
56. Sokpor, G., Brand-Saberi, B., Nguyen, H. P. & Tuoc, T. Regulation of Cell Delamination During Cortical Neurodevelopment and Implication for Brain Disorders. *Front. Neurosci.* **16**, 824802 (2022).
57. Gratton, M.-O. *et al.* Hes6 Promotes Cortical Neurogenesis and Inhibits Hes1 Transcription Repression Activity by Multiple Mechanisms. *Mol. Cell. Biol.* **23**, 6922–6935 (2003).
58. Murai, K., Philpott, A. & Jones, P. H. Hes6 Is Required for the Neurogenic Activity of Neurogenin and NeuroD. *PLoS ONE* **6**, e27880 (2011).
59. Sahara, S., Kawakami, Y., Izpisua Belmonte, J. C. & O'Leary, D. D. Sp8 exhibits reciprocal induction with Fgf8 but has an opposing effect on anterior-posterior cortical area patterning. *Neural Develop.* **2**, 10 (2007).
60. Borello, U. *et al.* Sp8 and COUP-TF1 Reciprocally Regulate Patterning and Fgf Signaling in Cortical Progenitors. *Cereb. Cortex* **24**, 1409–1421 (2014).
61. Bosone, C. *et al.* A polarized FGF8 source specifies frontotemporal signatures in spatially oriented cell populations of cortical assembloids. *Nat. Methods* **21**, 2147–2159 (2024).
62. Nita, A. *et al.* FGFR2 residence in primary cilia is necessary for epithelial cell signaling. *J. Cell Biol.* **224**, e202311030 (2025).
63. Demuynck, B. *et al.* Infigratinib low dose therapy is an effective strategy to treat hypochondroplasia. *J. Bone Miner. Res.* zjaf088 (2025) doi:10.1093/jbmr/zjaf088.
64. Behesti, H., Kocabas, A., Buchholz, D. E., Carroll, T. S. & Hatten, M. E. Altered temporal sequence of transcriptional regulators in the generation of human cerebellar granule cells. *eLife* **10**, e67074 (2021).
65. Arellano, J. I., Guadiana, S. M., Breunig, J. J., Rakic, P. & Sarkisian, M. R. Development and distribution of neuronal cilia in mouse neocortex. *J. Comp. Neurol.* **520**, 848–873 (2012).
66. Wu, J. Y. *et al.* Mapping of neuronal and glial primary cilia contactome and connectome in the human cerebral cortex. *Neuron* **112**, 41-55.e3 (2024).

1006 67. Neugebauer, J. M., Amack, J. D., Peterson, A. G., Bisgrove, B. W. & Yost, H. J. FGF signalling
1007 during embryo development regulates cilia length in diverse epithelia. *Nature* **458**, 651–
1008 654 (2009).
1009 68. Kunova Bosakova, M. *et al.* Regulation of ciliary function by fibroblast growth factor
1010 signaling identifies FGFR3-related disorders achondroplasia and thanatophoric dysplasia
1011 as ciliopathies. *Hum. Mol. Genet.* **27**, 1093–1105 (2018).
1012 69. Kunova Bosakova, M. *et al.* Fibroblast growth factor receptor influences primary cilium
1013 length through an interaction with intestinal cell kinase. *Proc Natl Acad Sci U A* **116**, 4316–
1014 4325 (2019).
1015 70. Liang, Y. *et al.* Transcription factors SP5 and SP8 drive primary cilia formation in
1016 mammalian embryos.
1017 71. Long, K. R. & Huttner, W. B. How the extracellular matrix shapes neural development.
1018 *Open Biol.* **9**, 180216 (2019).
1019 72. Álvarez, Z. *et al.* Artificial extracellular matrix scaffolds of mobile molecules enhance
1020 maturation of human stem cell-derived neurons. *Cell Stem Cell* **30**, 219-238.e14 (2023).
1021 73. Yang, L., Wei, M., Xing, B. & Zhang, C. Extracellular matrix and synapse formation. *Biosci.*
1022 *Rep.* **43**, BSR20212411 (2023).
1023 74. Joyner, A. L., Liu, A. & Millet, S. Otx2, Gbx2 and Fgf8 interact to position and maintain a
1024 mid–hindbrain organizer. *Curr. Opin. Cell Biol.* **12**, 736–741 (2000).
1025 75. Sato, T. & Joyner, A. L. The duration of *Fgf8* isthmic organizer expression is key to
1026 patterning different tectal-isthmo-cerebellum structures. *Development* **136**, 3617–3626
1027 (2009).
1028 76. Green, M. J. *et al.* Independently specified *Atoh1* domains define novel developmental
1029 compartments in rhombomere 1. *Development* **141**, 389–398 (2014).
1030 77. Suzuki-Hirano, A., Harada, H., Sato, T. & Nakamura, H. Activation of Ras-ERK pathway by
1031 Fgf8 and its downregulation by Sprouty2 for the isthmus organizing activity. *Dev. Biol.* **337**,
1032 284–293 (2010).
1033 78. Yu, T., Yaguchi, Y., Echevarria, D., Martinez, S. & Basson, M. A. Sprouty genes prevent
1034 excessive FGF signalling in multiple cell types throughout development of the cerebellum.
1035 *Development* **138**, 2957–2968 (2011).
1036 79. Del Corral, R. D., Breitkreuz, D. N. & Storey, K. G. Onset of neuronal differentiation is
1037 regulated by paraxial mesoderm and requires attenuation of FGF signalling. *Development*
1038 **129**, 1681–1691 (2002).
1039 80. Wilcock, A. C., Swedlow, J. R. & Storey, K. G. Mitotic spindle orientation distinguishes stem
1040 cell and terminal modes of neuron production in the early spinal cord. *Development* **134**,
1041 1943–1954 (2007).
1042 81. Olivera-Martinez, I. & Storey, K. G. Wnt signals provide a timing mechanism for the FGF-
1043 retinoid differentiation switch during vertebrate body axis extension. *Development* **134**,
1044 2125–2135 (2007).
1045 82. Lukaszewicz, A., Savatier, P., Cortay, V., Kennedy, H. & Dehay, C. Contrasting Effects of Basic
1046 Fibroblast Growth Factor and Neurotrophin 3 on Cell Cycle Kinetics of Mouse Cortical
1047 Stem Cells. *J. Neurosci.* **22**, 6610–6622 (2002).
1048 83. Gantner, C. W. *et al.* FGF-MAPK signaling regulates human deep-layer corticogenesis.
1049 *Stem Cell Rep.* **16**, 1262–1275 (2021).
1050 84. Basson, M. A. *et al.* Specific regions within the embryonic midbrain and cerebellum
1051 require different levels of FGF signaling during development. *Development* **136**, 1962–
1052 1962 (2009).

85. Catala, M. Development of the Central Nervous System. in *Textbook of Pediatric Neurosurgery* (eds Di Rocco, C., Pang, D. & Rutka, J. T.) 1–99 (Springer International Publishing, Cham, 2019). doi:10.1007/978-3-319-31512-6_1-1.
86. Watson, C., Shimogori, T. & Puelles, L. Mouse *Fgf8* -Cre-LacZ lineage analysis defines the territory of the postnatal mammalian isthmus. *J. Comp. Neurol.* **525**, 2782–2799 (2017).
87. Kasberg, A. D., Brunskill, E. W. & Steven Potter, S. SP8 regulates signaling centers during craniofacial development. *Dev. Biol.* **381**, 312–323 (2013).
88. Wagner, A. E. *et al.* SP8 Promotes an Aggressive Phenotype in Hepatoblastoma via FGF8 Activation. *Cancers* **12**, (2020).
89. Hämmerle, B. *et al.* Transient expression of Mnb/Dyrk1a couples cell cycle exit and differentiation of neuronal precursors by inducing p27KIP1 expression and suppressing NOTCH signaling. *Development* **138**, 2543–2554 (2011).
90. Sudarov, A. *et al.* Ascl1 Genetics Reveals Insights into Cerebellum Local Circuit Assembly. *J. Neurosci.* **31**, 11055 (2011).
91. Cerrato, V. *et al.* Multiple origins and modularity in the spatiotemporal emergence of cerebellar astrocyte heterogeneity. *PLOS Biol.* **16**, e2005513 (2018).
92. Louvi, A., Alexandre, P., Métin, C., Wurst, W. & Wassef, M. The isthmic neuroepithelium is essential for cerebellar midline fusion. *Development* **130**, 5319–5330 (2003).
93. Waas, B. *et al.* Dual and opposing roles for the kinesin-2 motor, KIF17, in Hedgehog-dependent cerebellar development. *Sci. Adv.* **10**, eade1650.
94. Jiwani, T., Kim, J. J. & Rosenblum, N. D. Suppressor of Fused (Sufu) controls cerebellum granule cell proliferation by suppressing Fgf8 and spatially regulating Gli proteins. *Development* dev.170274 (2020) doi:10.1242/dev.170274.
95. Kim, J. J. *et al.* Suppressor of Fused Controls Mid-Hindbrain Patterning and Cerebellar Morphogenesis via GLI3 Repressor. *J. Neurosci.* **31**, 1825–1836 (2011).
96. Yabut, O. R. *et al.* Aberrant FGF signaling promotes granule neuron precursor expansion in SHH subgroup infantile medulloblastoma. https://doi.org/10.7554/elife.100767.2 (2024) doi:10.7554/elife.100767.2.
97. De Mori, R. *et al.* Hypomorphic Recessive Variants in SUFU Impair the Sonic Hedgehog Pathway and Cause Joubert Syndrome with Cranio-facial and Skeletal Defects. *Am. J. Hum. Genet.* **101**, 552–563 (2017).
98. Serpieri, V. *et al.* SUFU haploinsufficiency causes a recognisable neurodevelopmental phenotype at the mild end of the Joubert syndrome spectrum. *J. Med. Genet.* **59**, 888 (2022).
99. Brugières, L. *et al.* High Frequency of Germline SUFU Mutations in Children With Desmoplastic/Nodular Medulloblastoma Younger Than 3 Years of Age. *J. Clin. Oncol.* **30**, 2087–2093 (2012).
100. Guerrini-Rousseau, L. *et al.* Germline SUFU mutation carriers and medulloblastoma: clinical characteristics, cancer risk, and prognosis. *Neuro-Oncol.* **20**, 1122–1132 (2018).
101. Roepman, R. *et al.* Interaction of nephrocystin-4 and RPGRIP1 is disrupted by nephronophthisis or Leber congenital amaurosis-associated mutations. *Proc. Natl. Acad. Sci.* **102**, 18520–18525 (2005).
102. Arts, H. H. *et al.* Mutations in the gene encoding the basal body protein RPGRIP1L, a nephrocystin-4 interactor, cause Joubert syndrome. *Nat. Genet.* **39**, 882–888 (2007).
103. Sang, L. *et al.* Mapping the NPHP-JBTS-MKS Protein Network Reveals Ciliopathy Disease Genes and Pathways. *Cell* **145**, 513–528 (2011).

104. Poretti, A. *et al.* Joubert syndrome: neuroimaging findings in 110 patients in correlation with cognitive function and genetic cause. *J. Med. Genet.* **54**, 521 (2017).
105. Dobin, A. *et al.* STAR: ultrafast universal RNA-seq aligner. *Bioinformatics* **29**, 15–21 (2013).
106. Ewels, P., Magnusson, M., Lundin, S. & Käller, M. MultiQC: summarize analysis results for multiple tools and samples in a single report. *Bioinformatics* **32**, 3047–3048 (2016).
107. Liao, Y., Smyth, G. K. & Shi, W. featureCounts: an efficient general purpose program for assigning sequence reads to genomic features. *Bioinformatics* **30**, 923–930 (2014).
108. Love, M. I., Huber, W. & Anders, S. Moderated estimation of fold change and dispersion for RNA-seq data with DESeq2. *Genome Biol.* **15**, 550 (2014).
109. Zink, R. C., Wolfinger, R. D. & Mann, G. Summarizing the incidence of adverse events using volcano plots and time intervals. *Clin. Trials* **10**, 398–406 (2013).
110. Zhou, Y. *et al.* Metascape provides a biologist-oriented resource for the analysis of systems-level datasets. *Nat. Commun.* **10**, 1523 (2019).

1142 **FIGURE 1. *RPGRIP1L*-deficient cerebellar organoids present a severe reduction of Purkinje**
1143 **cell markers and a mild decrease of glutamatergic lineage markers**
1144 **(A)** Diagram of the 3D cerebellar differentiation protocol. Time-line and drugs (SB: SMAD
1145 antagonists SB-431542; FGF2: Fibroblast growth factor 2; FGF19: Fibroblast growth factor 19;
1146 SDF1: stromal cell-derived factor 1) are indicated on top, culture media at the bottom. The
1147 blue circular arrow on top indicates orbital rotation. Protocol modified after [39] **(B)** Schematic
1148 representation of the RPGRIP1L protein and relative position of the mutations present in hiPSC
1149 lines. In both *RPGRIP1L* KO lines (Ph2 in purple, Wtc11 in pink) homozygous frameshift
1150 mutations result in premature stop codon before the first coiled-coil (CC) domain. JBTS patient
1151 (NG2266 in green) variants p.Q684X and c.2304+1G>T result in stop codons between the first
1152 and the second C2 domain. **(C)** Brain marker gene expression in cerebellar organoids at day 7.
1153 Heatmap based on the normalized expression values of selected brain marker genes. Z score
1154 was calculated on the log2(tpm+1) data from the bulk RNASeq analysis. Right: scheme of the
1155 gene expression domains in the E9.5 mouse brain. MHB: midbrain-hindbrain boundary.
1156 Thinner box for Wnt1: expression restricted to the roof plate. See supplementary Table 1 for
1157 number of independent experimental replicates (N) and sample numbering. **(D, E)** Graphs
1158 showing temporal gene expression analysis of Purkinje lineage markers (*OLIG2* and *CALB1*) (D)
1159 and glutamatergic lineage markers (*BARHL1* and *ATOH1*) (E) in control (blue), *RPGRIP1L* KO
1160 (magenta), and JBTS patient-derived (green) organoids throughout differentiation. Normalized
1161 gene expression (Log2(tpm+1)) values from bulk RNASeq analysis are displayed as mean ±
1162 SEM. More than 20 organoids were analyzed per condition per experiment. For control and
1163 *RPGRIP1L* KO, data were obtained from both Ph2 and Wtc11 lines. Day 0 (hiPSCs): N=2 for
1164 controls, N=2 for RPGRIP1L KO, N=1 for JBTS patient line; day 7-35 organoids: see
1165 Supplementary Table 2 for number of independent experimental replicates. **(F)**
1166 Immunofluorescence for OLIG2 (Purkinje lineage progenitors) on cryosections from control,
1167 *RPGRIP1L* KO and JBTS patient organoids at day 21. **(G)** Graph showing the % of OLIG2+ over
1168 DAPI+ nuclei. Each dot represents an organoid section. Several sections from different
1169 organoids were analyzed per condition (N=1). Data are shown as mean ± SEM. Asterisks
1170 denote statistical significance according to One-Way ANOVA Kruskal-Wallis test with Dunn's
1171 correction (***P<0.0002 and ****P< 0.0001). **(H)** Immunofluorescence for CALB1 on
1172 cryosections from day 28 control, *RPGRIP1L* KO and JBTS patient organoids. **(I)** Quantification
1173 of the % of CALB1+ cells over DAPI+ nuclei, on > 15 sections from different organoids per

1174 experiment per condition (control and *RPGRIP1L* KO: Ph2 line N=2 – round dots; JBTS patient:
1175 NG2266 line N=2 – squared dots). Data are shown as mean ± SEM. Asterisks denote statistical
1176 significance according to One-Way ANOVA Kruskal-Wallis test with Dunn's correction
1177 (****P<0.0001). **(J)** Immunofluorescence for BARHL1 on cryosections from day 28 control,
1178 *RPGRIP1L* KO and JBTS patient organoids. **(K)** Quantification of the % of BARHL1+ over DAPI+
1179 nuclei, in > 15 sections from different organoids per experiment per condition (control and
1180 *RPGRIP1L* KO N=3: Ph2 line N=2 – round dots, Wtc11 line N=1 – triangular dots; JBTS patient:
1181 NG2266 line N=2 – squared dots). Data are shown as mean ± SEM. Asterisks denote statistical
1182 significance according to One-Way ANOVA Kruskal-Wallis test with Dunn's correction
1183 (****P<0.0001). N: number of independent experimental replicates. Scale bars: 100 µm in F,
1184 H and J.
1185
1186
1187 **FIGURE 2. Organoid size and area of SOX2$^+$/ZO1$^+$ progenitors are increased in *RPGRIP1L*-**
1188 **deficient cerebellar organoids.**
1189 **(A**) Representative bright field images of cerebellar organoids at the indicated time points. **(B)**
1190 Graph representing the organoid growth rate, measured every 7 days from day 7 to day 35.
1191 Data are shown as the mean ± SEM of average organoid area from several independent
1192 experiment (N=3 Ph2 line, N=3 Wtc11 line, N=3 NG2266 line, n=10-60 organoids analyzed per
1193 experiment per condition at each timepoint). For control and *RPGRIP1L* KO conditions, data
1194 from Ph2 and Wtc11 lines were pooled. Asterisks denote statistical significance according to
1195 Two-Way ANOVA test (*P<0.033, ***P<0.0002, ****P<0.0001). **(C)** Immunofluorescence for
1196 SOX2 neural progenitor marker (magenta) and ZO1 apical marker (green) on cryosections from
1197 control, *RPGRIP1L* KO and JBTS patient organoids at day 14. Examples of small neural rosettes
1198 are circled by dotted lines. **(D)** Quantification of the ZO1+ area over the DAPI+ area in sections
1199 from control, *RPGRIP1L* KO and JBTS patient organoids at day 14. Each dot represents an
1200 organoid section. Several sections from different organoids were analyzed per condition:
1201 control and *RPGRIP1L* KO: N=2 (Ph2 N=1 – round dots, Wtc11 N=1 – triangular dots), JBTS
1202 patient: NG2266 N=1 – squared dots. Mean ± SEM are indicated. Asterisks: statistical
1203 significance according to One-Way ANOVA Kruskal-Wallis test with Dunn's correction (****P<
1204 0.0001) **(E)** Graph showing the % of SOX2$^+$ cells in sections from control, *RPGRIP1L* KO and
1205 JBTS patient organoids at day 14. Each dot represents an organoid section. Several sections

1206 from different organoids were analyzed per condition: control and *RPGRIP1L* KO: N=3 (Ph2
1207 N=1 – round dots, Wtc11 N=2 – triangular dots), JBTS patient: NG2266 N=1 – squared dots.
1208 Mean ± SEM are indicated. Asterisks denote statistical significance according to One-Way
1209 ANOVA Kruskal-Wallis test with Dunn's correction (****P< 0.0001). N: number of independent
1210 experimental replicates. Scale bars: 500 µm in A and 100 µm in C.
1211
1212
1213 **FIGURE 3. Differential requirement of RPGRIP1L protein for ciliogenesis in apical and non-**
1214 **polarized neural progenitors.**
1215 **(A-C)** Immunofluorescence for INPP5E (green) and gamma-TUBULIN (magenta) on sections
1216 from control (A), *RPGRIP1L* KO (B) and JBTS patient (C) organoids at day 14. Scale bar, 10 µm.
1217 The schematic on the left represents the position of the scanned regions: i.e. internal lumen
1218 of neural rosettes. **(D)** Graph showing the quantification of ciliary length. Measures for
1219 individual cilia are represented and the mean value is indicated. Asterisks: statistical
1220 significance according to One-Way ANOVA Kruskal-Wallis with Dunn's correction (**P <
1221 0.0021)**. (E-G)** Immunofluorescence for INPP5E (green) and gamma-TUBULIN (magenta) on
1222 sections from control (E), *RPGRIP1L* KO (F) and JBTS patient (G) organoids at day 14. Scale bar,
1223 10 µm. The schematic on the left represents the position of the scanned regions: i.e. non-
1224 polarized tissue. **(H-J)** Graphs showing quantifications of ciliary properties in non-polarized
1225 areas of control, *RPGRIP1L* KO and JBTS patient cerebellar organoids. Asterisks denote
1226 statistical significance according to One-Way ANOVA Kruskal-Wallis test with Dunn's
1227 correction (**P < 0.0021, ****P < 0.0001). Control and *RPGRIP1L* KO: N=4 (Wtc11 N=3 –
1228 triangular dots, Ph2 N=1 – round dots); JBTS patient: NG2266 N=2 – squared dots. N: number
1229 of independent experimental replicates. In **(H)** Ciliary density is calculated as the % of gamma-
1230 TUBULIN+ basal bodies presenting an INPP5E+ axoneme over the total number of basal bodies
1231 per field. Each dot on the graph represents one quantified field representative for one
1232 organoid section. In **(I-J)** each dot represents one individual cilium. Average cilia length (I) and
1233 average axonemal INPP5E intensity after background subtraction (J) are calculated from >400
1234 cilia per condition measured in >20 organoids from independent experiments and hiPSC lines.
1235 Scale bars: 10 µm in A-C and E-G.
1236

1237 **FIGURE 4. Transcriptome analysis reveals early FGF signaling upregulation and neurogenesis**
1238 **impairment in *RPGRIP1L*-deficient cerebellar organoids**
1239 **(A, B)** Volcano plots representing differentially expressed genes (DEGs) resulting from DESeq2
1240 analysis (only genes with P<0.05; $|\log_2 FC|>1$ are colored) in *RPGRIP1L* KO versus control
1241 condition (A) or in JBTS patient versus control condition (B) at day 14. Selected genes from
1242 representative pathways and cellular processes are circled with different colors as indicated
1243 in the legend on the top right of the panels. **(C)** qPCR analysis of *FGF8* expression levels on
1244 cerebellar organoids at different timepoints; control and *RPGRIP1L* KO: N=6 (Ph2 N=2, Wtc11
1245 N=4); JBTS patient: N=2. Data are shown as individual values; mean ± SEM are indicated.
1246 Asterisks denote statistical significance according to ordinary Two-Way ANOVA performed on
1247 control and *RPGRIP1L* KO samples (*P<0.033, **P<0.0021, ***P<0.0002, ****P < 0.0001). N:
1248 number of independent experimental replicates. **(D)** Heatmap representing normalized RNA
1249 expression values of selected DEGs in control and *RPGRIP1L*-deficient cerebellar organoids
1250 over time. >20 organoids per replicate per condition were collected at each timepoint; See
1251 supplementary Table 2 for number of independent experiments and sample numbering. **(E)**
1252 Confocal images of immunofluorescence for SP8 (green) on cryosections from control and
1253 *RPGRIP1L*-deficient organoids at day 14. Nuclei are stained with DAPI (blue). Right: graph
1254 showing the % of SP8+ over DAPI+ nuclei, counted in > 10 sections from different organoids
1255 per condition per experiment. Controls and *RPGRIP1L* KO: N=3 (Wtc11 N=2 – triangular dots,
1256 Ph2 N=1 – circular dots), JBTS: NG2266 N=1 squared dots. Each dot in the graph represents
1257 one organoid; mean ± SEM are shown. Asterisks denote statistical significance according to
1258 One-Way ANOVA Kruskal-Wallis test with Dunn's correction (***P<0.0002; ****P<0.0001).
1259 Scale bar, 100 µm. N: number of independent experimental replicates. **(F)** High-resolution
1260 AIRYSCAN immunofluorescence images for pMEK1/2 (green), ARL13B (magenta) and gamma-
1261 TUBULIN (blue) on cryosections from control and *RPGRIP1L*-deficient organoids at day 14.
1262 Scale bar, 1 µm. Right: graph showing the mean % of pMEK1/2+ over gamma-TUBULIN+ basal
1263 bodies, counted in > 10 sections from different organoids per condition per experiment.
1264 Controls and *RPGRIP1L* KO: N=3 (Wtc11 N=2 – triangular dots, Ph2 N=1 – circular dots), JBTS:
1265 NG2266 N=1 squared dots. Each dot in the graph represents one section; mean ± SEM are
1266 shown. Asterisks denote statistical significance according to Welch's t test (*P<0.033,
1267 **P<0.0021). N: number of independent experimental replicates.
1268

1269 **FIGURE 5. *RPGRIP1L*-deficient organoids display severe neuronal maturation and**
1270 **extracellular matrix defects as shown by transcriptome analysis**
1271 **(A-B)** Volcano plots representing DEGs resulting from DESeq2 analysis (only genes with
1272 P<0.001, $|\log_2 FC|>2$ are colored) in *RPGRIP1L* KO versus control condition (A) or in JBTS
1273 patient versus control condition (B) at day 28. Selected genes involved in neuronal
1274 differentiation or in building ECM are circled with different colors as indicated in the legend
1275 on the top right of the panel. **(C)** Heatmap representing the normalized RNA expression values
1276 of selected differentially expressed genes in control and *RPGRIP1L*-deficient cerebellar
1277 organoids over time. 20 organoids were analyzed per condition. See supplementary Table 2
1278 for number of independent experiments and sample numbering. **(D, E)** Selected GO-terms
1279 overrepresented among *RPGRIP1L* KO (D) and JBTS patient (E) downregulated genes extracted
1280 from bulk RNA seq DESeq2 lists at day 28.
1281
1282 **FIGURE 6. Blocking FGF signaling with BGJ-398 drug rescues neurogenesis in *RPGRIP1L*-**
1283 **deficient cerebellar organoids.**
1284 **(A)** Scheme representing the experimental plan for organoid treatment with FGFR-inhibitor
1285 (BGJ-398) along the 3D cerebellar differentiation protocol. Bracket on the top represent the
1286 time-window of BGJ-398 treatment. **(B)** Graph representing the growth rate of cerebellar
1287 organoids (left) and representative bright field images of cerebellar organoids at day 28 (right).
1288 Organoid area was measured every 7 days from day 7 to day 35 of the differentiation protocol.
1289 Data are shown as the mean ± SEM of average organoid area from several independent
1290 experiments. Control and *RPGRIP1L* KO: N=3 (Wtc11), JBTS patient: N=1 (NG2266 line); n=10-
1291 60 organoids analyzed per experiment per condition. Scale bar, 500 µm. **(C, D)** Heatmaps
1292 representing the normalized RNA expression values over time of selected DEGs in control and
1293 *RPGRIP1L* KO (C) or control and JBTS patient-derived (D) cerebellar organoids, untreated or
1294 treated with BGJ-398. For sample numbering and number of independent experiments see
1295 Supplementary Table 3 (for C) and Supplementary Table 4 (for D). At least 20 organoids were
1296 analyzed per condition per experiment. **(E)** Immunofluorescence for SOX2 (gray), NEUROD1
1297 (green) and HUC/D (magenta) on cryosections from control and *RPGRIP1L*-deficient organoids
1298 untreated or treated with BGJ-398 at day 14. Nuclei are stained with DAPI (blue). Scale bar,
1299 100 µm. **(F-H)** Graphs showing the % of NEUROD1+ (F), HUC/D+ (G) and SOX2+ (H) cells over
1300 DAPI+ nuclei., counted in > 15 sections from different organoids per condition per experiment.

1301 Controls and *RPGRIP1L* KO: N=3 (Wtc11 N=2 – triangular dots, Ph2 N=1 – circular dots), JBTS:
1302 NG2266 N=1 squared dots. Each dot in the graph represents one organoid; mean ± SEM are
1303 shown. Asterisks denote statistical significance according to One-Way ANOVA Kruskal-Wallis
1304 test with Dunn's correction (**P<0.0021; ****P<0.0001). N: number of independent
1305 experimental replicates.
1306
1307 **FIGURE 7. Neural progenitor proliferation is increased in *RPGRIP1L*-deficient organoids and**
1308 **can be rescued by blocking FGF signaling without restoring cilia features**
1309 **(A)** Left: Immunofluorescence for SP8 (green) on cryosections from day 21 control and
1310 *RPGRIP1L*-deficient organoids untreated or treated with BGJ-398. Nuclei are stained with
1311 DAPI. Scale bar, 100 µm. Right: Graph showing the % of SP8+ over DAPI+ nuclei, counted in
1312 several sections from different organoids per condition. Controls and *RPGRIP1L* KO: N=3
1313 (Wtc11 N=2 – triangular dots, Ph2 N=1 – circular dots), JBTS: NG2266 N=1 squared dots. Each
1314 dot in the graph represents one organoid; mean ± SEM are shown. Asterisks denote statistical
1315 significance according to One-Way ANOVA Kruskal-Wallis test with Dunn's correction
1316 (*P<0.033; ***P<0.0002; ****P<0.0001). **(B)** Graph showing the relative mean intensity of
1317 pMEK1/2 labeling adjacent to gamma-Tubulin+ basal bodies, quantified in > 10 sections from
1318 different organoids per condition per experiment. Controls and *RPGRIP1L* KO: N=3 (Wtc11 N=2
1319 – triangular dots, Ph2 N=1 – circular dots), JBTS: NG2266 N=1 squared dots. Each dot in the
1320 graph represents the mean of all pMEK1/2 ROIs measured in one field (one organoid) ; mean
1321 of the means ± SEM are shown. Asterisks denote statistical significance according to Welch's
1322 t test (***P<0.0002; ****P<0.0001). N: number of independent experimental replicates. **(C-**
1323 **E)** Graphs showing the quantification of cilia density (C), ciliary length (D) and INPP5E amount
1324 in cilia (E) in control and *RPGRIP1L*-deficient organoids treated or not with BGJ-398. For cilia
1325 density, each dot in the graph represents one organoid; mean ± SEM are shown. For cilia
1326 length and INPP5E amount, measures for individual cilia (>200) are represented and the mean
1327 value is indicated. Asterisks: statistical significance according to One-Way ANOVA Kruskal-
1328 Wallis with Dunn's correction (****P<0.0001)**.** Control and *RPGRIP1L* KO treated with BGJ:
1329 N=2 Wtc11 – triangular dots; JBTS patient: NG2266 N=1 – squared dots. N: number of
1330 independent experimental replicates. **(F)** Immunofluorescence for SOX2 (magenta), HUC/D
1331 (blue) and EdU (green) on organoid cryosections at day 23 – 5 days after the 2h EdU pulse
1332 (chase experiment), from control and *RPGRIP1L*-deficient organoids untreated or treated with

1333 BGJ-398. **(G, H)** Graphs showing the % of EdU+ cells over the DAPI+ nuclei (G) and the % of
1334 EdU+/SOX2+ cells over the total number of SOX2+ cells (H) at day 23 (chase experiment). Cells
1335 were counted in several sections from different organoids per condition. Control and
1336 *RPGRIP1L* KO: N=1 (Wtc11); JBTS: N=1 (NG2266). Each dot in the graph represents one
1337 organoid; mean ± SEM are shown. Asterisks: statistical significance according to Ordinary-Way
1338 ANOVA after normal distribution testing (**P<0.0021; ****P<0.0001) **(I)** Graph showing the
1339 ratio between "strong" and "faint" EdU labeling in the % of EdU+ cells over total nuclei. Mean
1340 ± SEM are shown. N: number of independent experimental replicates. Scale bars: 100 µm.
1341
1342
1343
1344
1345
1346
1347
1348
1349
1350
1351
1352
1353
1354
1355
1356
1357
1358
1359
1360
1361
1362
1363

1364 **Supplementary Figure 1. Cerebellar organoids generated from control human induced**
1365 **pluripotent stem cells recapitulate early steps of cerebellar development**
1366 **(A-C)** Immunofluorescence for SOX2 (magenta, neural progenitors) and HUC/D (green, early-
1367 born neurons) on cryosections from control organoids at indicated time-points. Nuclei are
1368 stained with DAPI (blue). **(D-G)** Graph showing normalized temporal gene expression analysis
1369 from bulk RNAseq data **(D)**: Purkinje cell markers: OLIG2, SKOR2, CALB1, **(E)** Glutamatergic
1370 lineage markers BARHL1, PAX6, ATOH1, **(F)** Granule Neuron marker (*GABRA6)*, and **(G)** *SHH*.
1371 Data are displayed as mean ± SEM and were obtained from both Ph2 and Wtc11 cell lines. Day
1372 0 (hiPSCs): N=2; day 7-35 organoids: see Supplementary Table 2 for number of independent
1373 experimental replicates. **(H)** Immunofluorescence for BARHL1 (glutamatergic lineage marker)
1374 and CALB1 (Purkinje cell marker) on day 28 control organoid cryosection. Scale bars: 100 µm
1375 in A-C and H.
1376
1377 **Supplementary Figure 2. Altered RNA expression of Purkinje cell and glutamatergic lineage**
1378 **markers in *RPGRIP1L*-deficient cerebellar organoids**
1379 **(A-C')** Immunofluorescence on cryosections from control (A, A'), *RPGRIP1L* KO (B, B') and JBTS
1380 patient (C, C') organoids at day 21, labeling RPGRIP1L (in green) and the ciliary marker ARL13B
1381 (in magenta). Nuclei are stained with DAPI in A,B,C (blue) and basal bodies are stained with
1382 GTUB in A', B', C' (blue). Scale bars: 10 µm in A-C and 2 µm in A'-C'. **(D)** Graph showing
1383 normalized temporal gene expression analysis from bulk RNAseq data, displayed as mean ±
1384 SEM, of the Purkinje lineage markers *SKOR2, FOXP2, PDE1C* and *ITPR1* along the differentiation
1385 protocol. For control and *RPGRIP1L* KO conditions data were obtained from both Ph2 and
1386 Wtc11 cell lines. See Supplementary Table 2 for number of independent experimental
1387 replicates. **(E-F)** qPCR analysis of (E) the PC markers *OLIG2, SKOR2* and *CALB1* and (F) the
1388 glutamatergic lineage markers *PAX6, BARHL1, ATOH1*, in cerebellar organoids at different
1389 timepoints from several independent experiments. Each dot in the graph represents one
1390 independent experiment per timepoint and condition; circular dots represent Ph2 line,
1391 triangular dots represent Wtc11 line, squared dots represent NG2266 line. Mean ± SEM are
1392 shown. Asterisks denote statistical significance according to ordinary Two-Way ANOVA
1393 (*P<0.033, **P < 0.0021, ***P<0.0002 and ****P< 0.0001). **(G)** Immunofluorescence for
1394 ATOH1 (glutamatergic lineage) on cryosections from control, *RPGRIP1L* KO and JBTS patient
1395 organoids at day 28. **(H)** Graph showing the % of ATOH1-positive cells over the total number

1396 of nuclei stained with DAPI. Positive cells were counted in more than 15 sections from
1397 different organoids per experiment per condition. Control and *RPGRIP1L* KO: N=3 (Ph2 N=2 –
1398 circular dots, Wtc11 N=1 – triangular dots); JBTS patient: NG2266 N=2 – squared dots. Each
1399 dot in the graph represent one organoid. Mean ± SEM are indicated. Asterisks denote
1400 statistical significance according to One-Way ANOVA Kruskal-Wallis test with Dunn's
1401 correction (****P<0.0001). **(I-K)** Graphs showing the average intensity of CALB1 (I), BARHL1
1402 (J), ATOH1 (K) labeling on cryosections from control, *RPGRIP1L* KO and JBTS organoids at day
1403 28. Average cell intensity was measured in more than 15 sections from different organoids per
1404 experiment per condition. Relative mean intensity was calculated considering the mean
1405 intensity in control organoid sections as the reference value (1). Each dot in the graph
1406 represent one organoid. Mean ± SEM are indicated;. Asterisks denote statistical significance
1407 according to One-Way ANOVA Kruskal-Wallis test with Dunn's correction (*P<0.033, and
1408 ****P<0.0001). N: number of independent experimental replicates. Scale bars: 100 µm in H.
1409
1410 **Supplementary Figure 3. FGF8 protein localization at the apical sides of early neural**
1411 **progenitors**
1412 **(A, B)** Confocal images of immunofluorescence labeling ZO1 (magenta) and FGF8 (green) on
1413 cryosections from day 14 control, *RPGRIP1L* KO and JBTS patient organoids. Accumulation of
1414 FGF8 protein is visible at ZO1+ apical sides of progenitor rosettes in control, *RPGRIP1L* KO and
1415 JBTS patient organoids (A), as well as at ZO1+ apical junctions at the organoid borders in
1416 *RPGRIP1L* KO and JBTS patient organoids (B). **(C)** Large field confocal images of
1417 immunofluorescence on organoid sections for pMEK1/2 (green) showing pMEK1/2
1418 localization at the cilium base in non-dividing cells, and at the spindle poles in dividing cells
1419 (stars). Top images: non polarized organoid regions; bottom images: polarized rosettes. Scale
1420 bars: 10 µm in A-C.
1421
1422 **Supplementary Figure 4. FGF signaling inhibition rescues organoid size and gene expression**
1423 **in *RPGRIP1L* deficient organoids.**
1424 **(A-B)** Heatmap representation of the normalized gene expression values of selected
1425 differentially expressed genes in control and in *RPGRIP1L* KO cerebellar organoids untreated
1426 or treated with BGJ-398 (A) and JBTS patient-derived cerebellar organoids untreated or
1427 treated with BGJ-398 (B). See supplementary Table 3 for number of independent experiments

1428 and sample numbering in A and see supplementary Table 4 for number of independent
1429 experiments and sample numbering in B. **(C-J)** Graphs showing gene expression levels at
1430 different timepoints by qPCR analysis of *FGF8* (C), *ETV4* (D) *ETV5* (E), *SPRY1* (F), *NEUROD1* (G),
1431 *NEUROG1* (H), *SKOR2* (I) and *CALB1* (J) in control and *RPGRIP1L*-deficient cerebellar organoids
1432 untreated or treated with BGJ-398. Data are shown as individual values from independent
1433 experiments, mean ± SEM are indicated. For (C-E, J) control and *RPGRIP1L* KO: N=4 (Wtc11);
1434 JBTS patient: N=2 (NG2266). For (F-I) control and *RPGRIP1L* KO: N=3 (Wtc11); JBTS patient:
1435 N=1 (NG2266). N: number of independent experimental replicates.
1436 **(K)** Left: Immunofluorescence for OLIG2 (green) on cryosections from day 21 control and
1437 *RPGRIP1L*-deficient organoids untreated or treated with BGJ-398. Nuclei are stained with DAPI
1438 (blue). Scale bar, 100 µm. Right: Graph showing the % of OLIG2+ over DAPI+ nuclei, counted
1439 in several sections from different organoids per condition. Controls and *RPGRIP1L* KO: N=1
1440 (Ph2 N=1); JBTS: NG2266 N=1. Each dot in the graph represents one organoid; mean ± SEM
1441 are shown. Asterisks denote statistical significance according to One-Way ANOVA Kruskal-
1442 Wallis test with Dunn's correction (**P<0.0021; ***P<0.0002). N: number of independent
1443 experimental replicates.
1444
1445 **Supplementary Figure 5. EdU incorporation experiment shows that neural progenitor**
1446 **proliferation is increased in *RPGRIP1L*-deficient organoids and can be partially rescued by**
1447 **blocking FGF signaling.**
1448 **(A)** Immunofluorescence for SOX2 (magenta) and EdU (green) on organoid cryosections at day
1449 18 – 2h after EdU pulse, from control and *RPGRIP1L*-deficient organoids, untreated or treated
1450 with BGJ-398. **(B, C)** Graphs showing the % of EdU+ cells over the DAPI+ nuclei (B) and the %
1451 of EdU+SOX2+ cells over the total number of SOX2+ cells (C) at day 18 – 2h after EdU pulse,
1452 counted in several sections from different organoids per condition. Control and *RPGRIP1L* KO:
1453 N=1 (Wtc11); JBTS: N=1 (NG2266). Each dot in the graph represents one organoid; mean ±
1454 SEM are shown. Asterisks: statistical significance according to Ordinary-Way ANOVA after
1455 normal distribution testing (*P<0.033; ****P<0.0001).
1456
1457 **Supplementary Figure 6. NG2266 splice variant c.2304+1G>T results in intron retention**.
1458 **(A)** Schematic representation of *RPGRIP1L* gene exons 14-18 and PCR primers position to
1459 analyze cDNA products of *RPGRIP1L* gene in JBTS patient cells (NG2266 line) compared to

1460 control (Ph2 line). **(B)** PCR products from JBTS patient and control cerebellar cDNAs,
1461 templated by primer pairs as indicated, were analyzed by agarose gel electrophoresis and
1462 visualized with ethidium bromide. The primer pair 1-2 only amplifies JBTS patient cDNA,
1463 showing intron 16-17 retention. The primer pair 1-3 amplify both the second JBTS patient
1464 allele (encoding the *RPGRIP1L* Q684X variant) and control cDNA. **(C)** Sequence of the PCR
1465 product templated by primer pair 1-2 on cDNA derived from

Figure 1

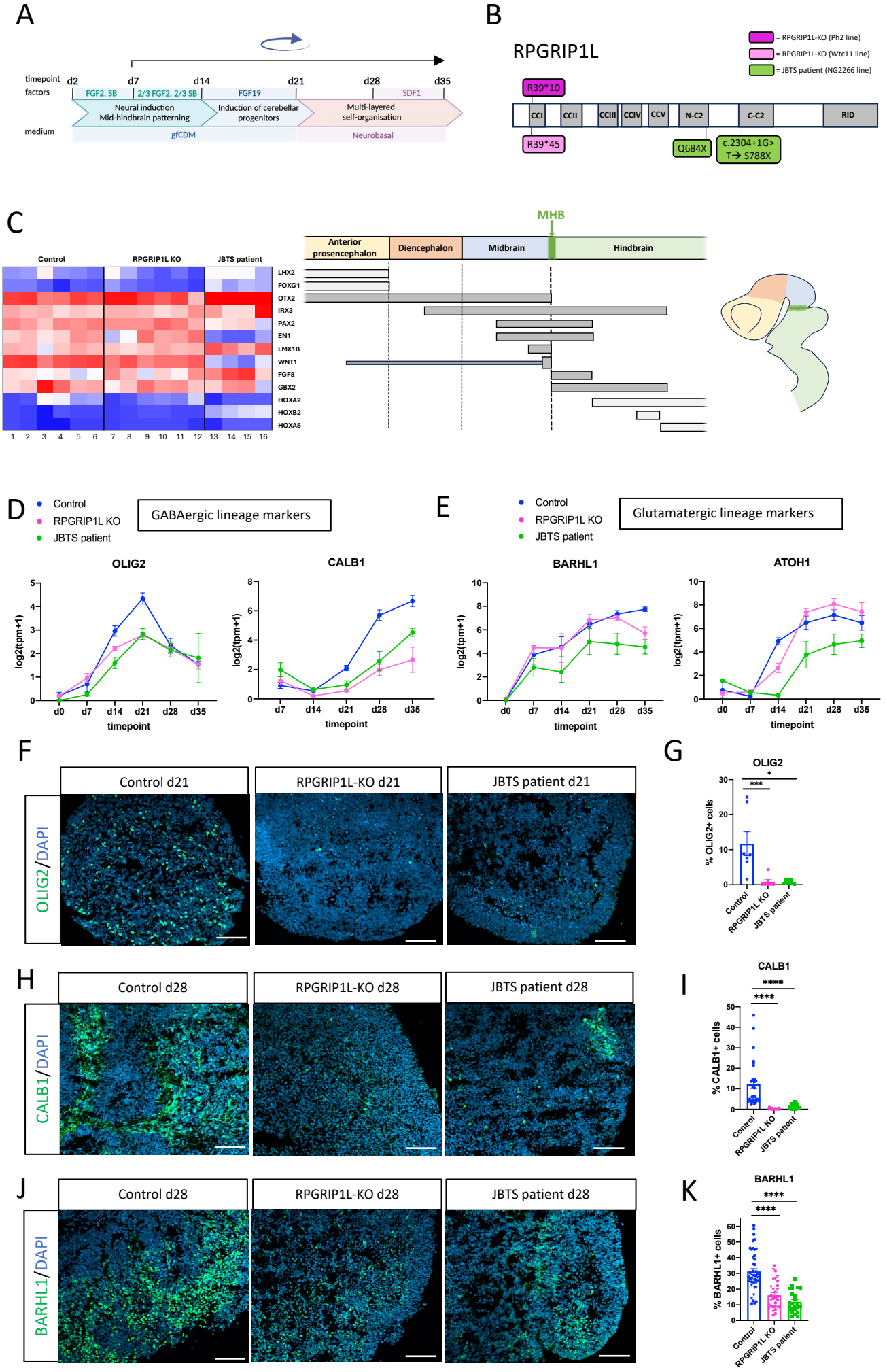
A
timepoint
factors
medium
d2
d7
d14
d21
d28
d35
FGF2, SB
2/3 FGF2, 2/3 SB
FGF19
SDF1
Neural induction
Mid-hindbrain patterning
Induction of cerebellar progenitors
Multi-layered self-organisation
gfCDM
Neurobasal
B
RPGRIP1L
= RPGRIP1L-KO (Ph2 line)
= RPGRIP1L-KO (Wtc11 line)
= JBTS patient (NG2266 line)
R39*10
R39*45
CCI
CCII
CCIII
CCIV
CCV
N-C2
C-C2
RID
Q684X
c.2304+1G> T→ S788X
C
Control
RPGRIP1L KO
JBTS patient
MHB
Anterior prosencephalon
Diencephalon
Midbrain
Hindbrain
LHX2
FOXG1
OTX2
IRX3
PAX2
EN1
LMX1B
WNT1
FGF8
GBX2
HOXA2
HOXB2
HOXA5
D
Control
RPGRIP1L KO
JBTS patient
GABAergic lineage markers
OLIG2
CALB1
log2(tpm+1)
timepoint
E
Glutamatergic lineage markers
BARHL1
ATOH1
F
Control d21
RPGRIP1L-KO d21
JBTS patient d21
OLIG2/DAPI
G
OLIG2
% OLIG2+ cells
H
Control d28
RPGRIP1L-KO d28
JBTS patient d28
CALB1/DAPI
I
CALB1
% CALB1+ cells
J
Control d28
RPGRIP1L-KO d28
JBTS patient d28
BARHL1/DAPI
K
BARHL1
% BARHL1+ cells

Supplementary Figure 1

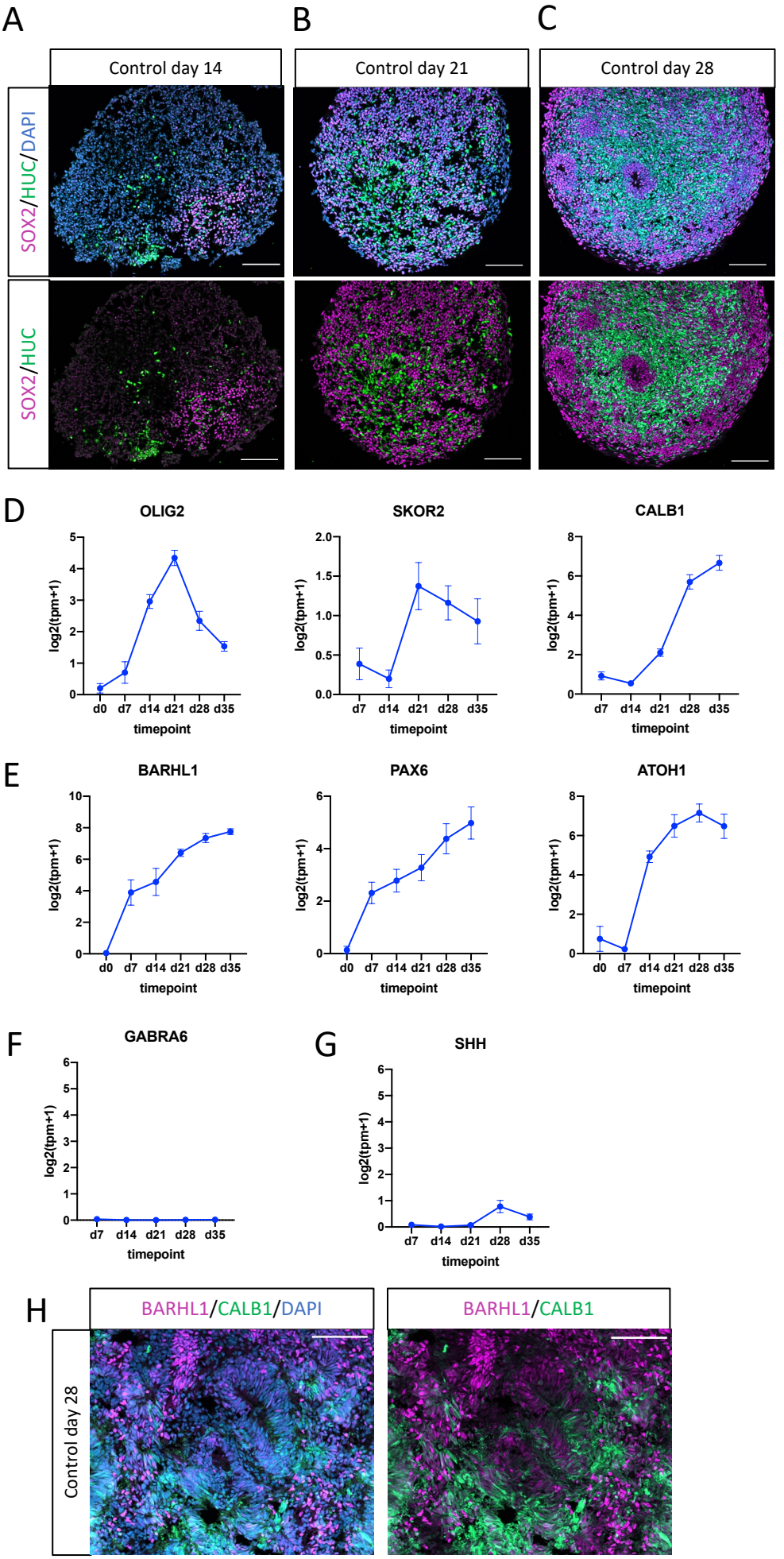

Supplementary Figure 2

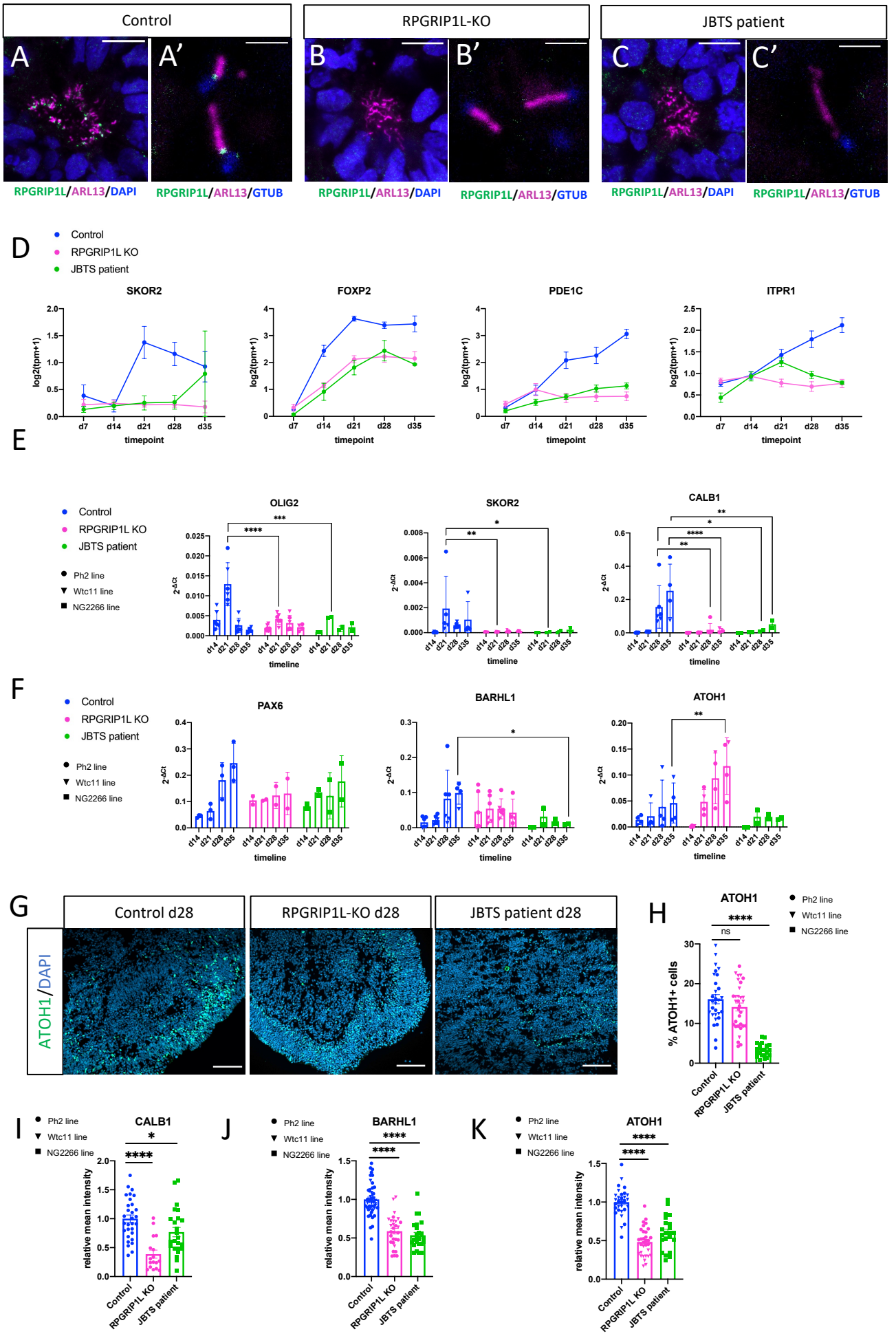

Figure 2

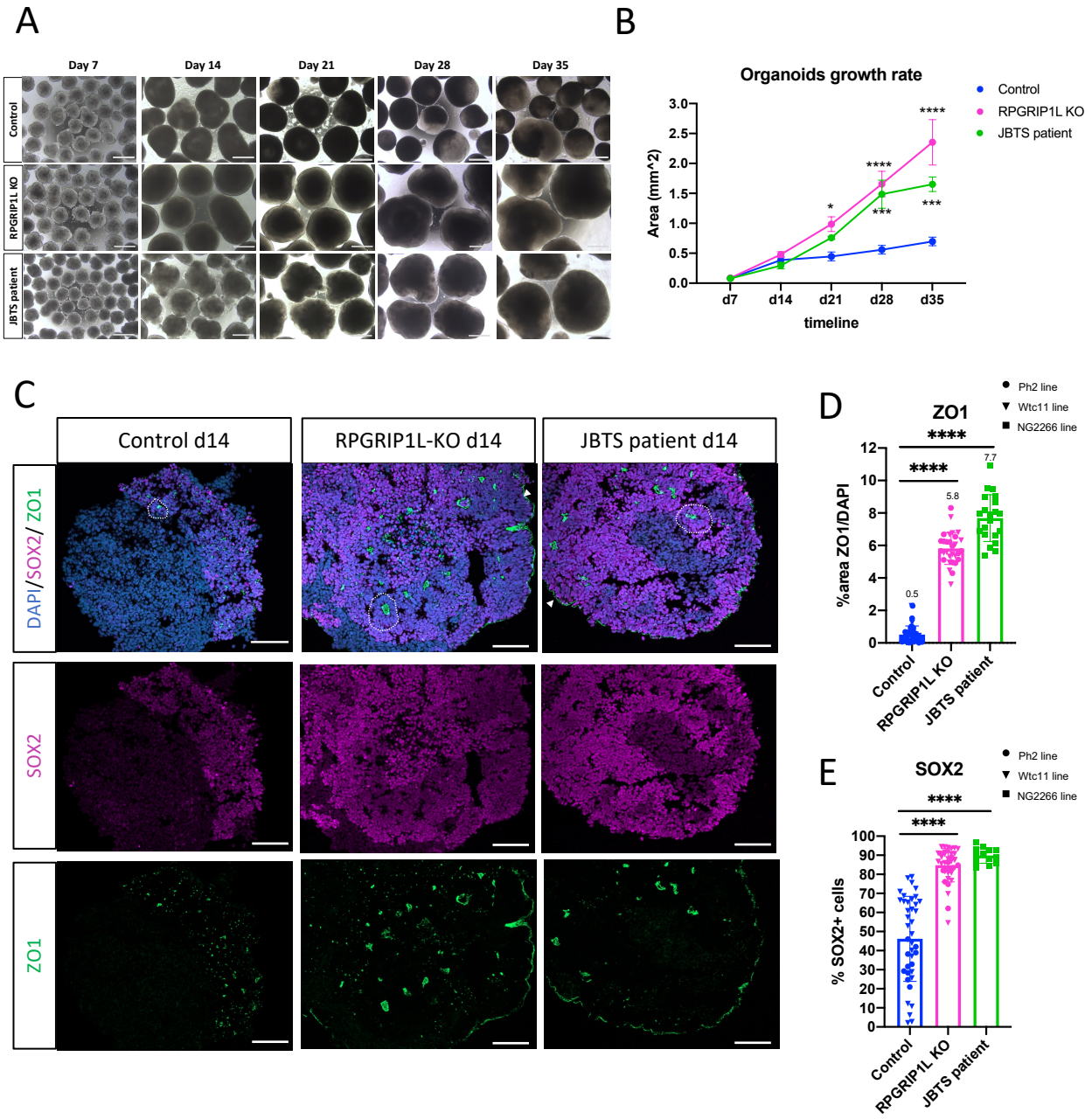
A
Day 7
Day 14
Day 21
Day 28
Day 35
Control
RPGRIP1L KO
JBTS patient
B
Organoids growth rate
Area (mm^2)
timeline
d7
d14
d21
d28
d35
Control
RPGRIP1L KO
JBTS patient
C
Control d14
RPGRIP1L-KO d14
JBTS patient d14
DAPI/SOX2/ ZO1
SOX2
ZO1
D
ZO1
%area ZO1/DAPI
Ph2 line
Wtc11 line
NG2266 line
Control
RPGRIP1L KO
JBTS patient
E
SOX2
% SOX2+ cells
Ph2 line
Wtc11 line
NG2266 line
Control
RPGRIP1L KO
JBTS patient

Figure 3

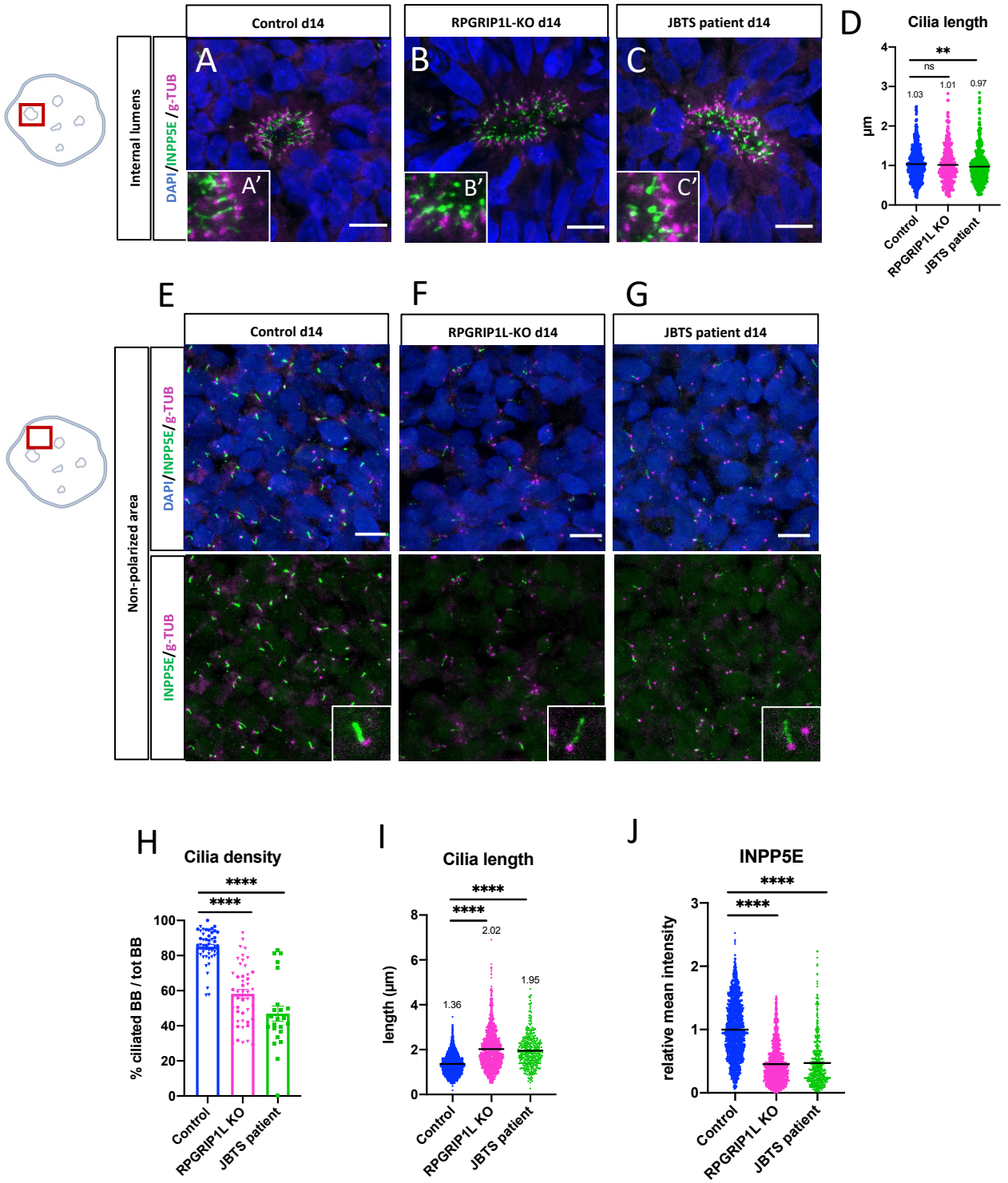
Control d14
RPGRIP1L-KO d14
JBTS patient d14
Internal lumens
DAPI/INPPSE/g-TUB
A
A'
B
B'
C
C'
D
Cilia length
µm
**
ns
1.03
1.01
0.97
Control
RPGRIP1L KO
JBTS patient
E
F
G
Non-polarized area
DAPI/INPP5E/g-TUB
INPP5E/g-TUB
H
Cilia density
% ciliated BB / tot BB
****
****
I
Cilia length
length (µm)
****
****
1.36
2.02
1.95
J
INPP5E
relative mean intensity
****
****

Figure 4

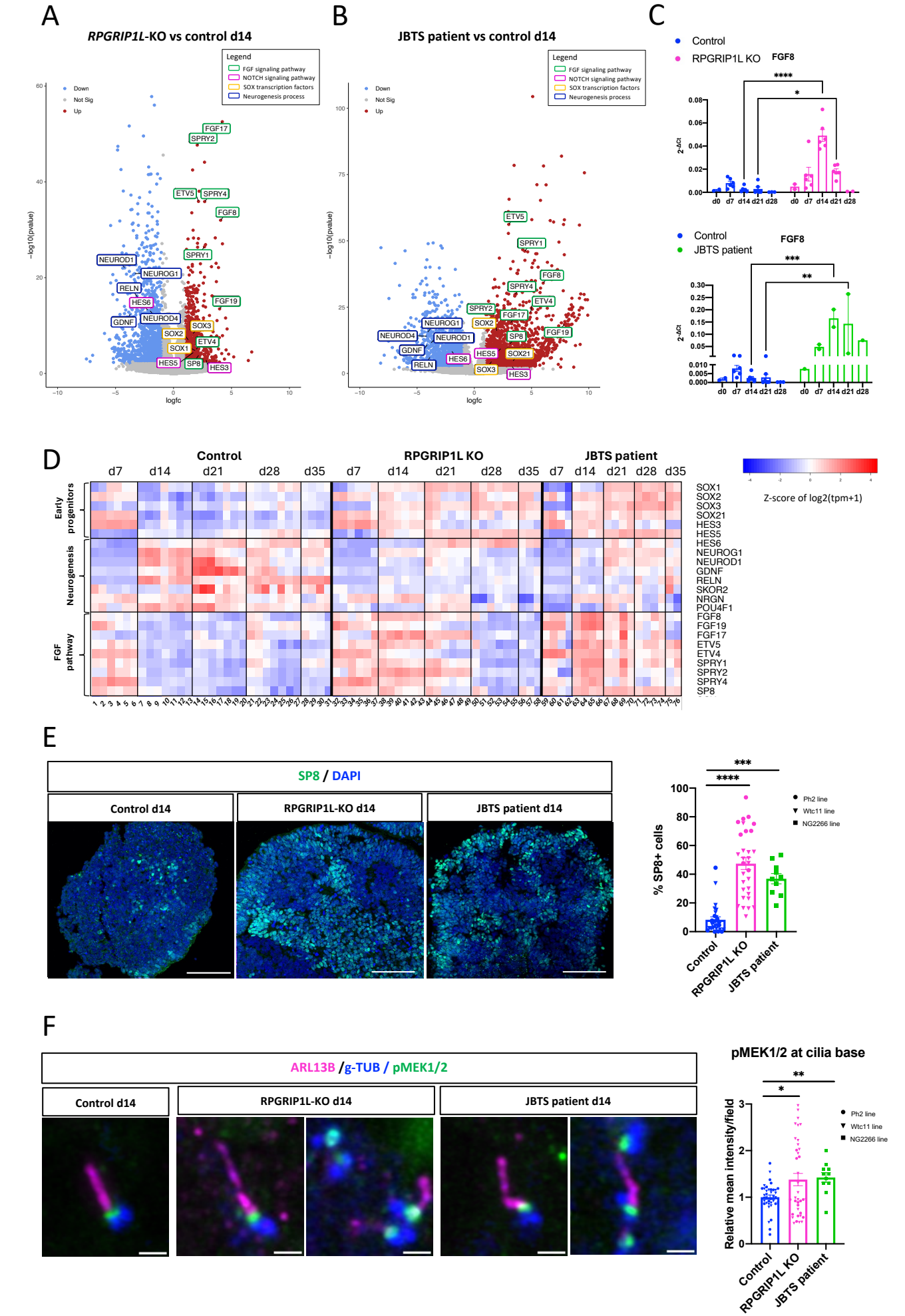
A
RPGRIP1L-KO vs control d14
Legend
FGF signaling pathway
NOTCH signaling pathway
SOX transcription factors
Neurogenesis process
Down
Not Sig
Up
−log10(pvalue)
logfc
B
JBTS patient vs control d14
C
Control
RPGRIP1L KO
FGF8
JBTS patient
2^-ΔCt
d0 d7 d14 d21 d28
D
Control
RPGRIP1L KO
JBTS patient
d7 d14 d21 d28 d35
Early progenitors
Neurogenesis
FGF pathway
Z-score of log2(tpm+1)
SOX1
SOX2
SOX3
SOX21
HES3
HES5
HES6
NEUROG1
NEUROD1
GDNF
RELN
SKOR2
NRGN
POU4F1
FGF8
FGF19
FGF17
ETV5
ETV4
SPRY1
SPRY2
SPRY4
SP8
E
SP8 / DAPI
Control d14
RPGRIP1L-KO d14
JBTS patient d14
% SP8+ cells
Ph2 line
Wtc11 line
NG2266 line
Control
RPGRIP1L KO
JBTS patient
F
ARL13B /g-TUB / pMEK1/2
Control d14
RPGRIP1L-KO d14
JBTS patient d14
pMEK1/2 at cilia base
Relative mean intensity/field

Supplementary Figure 3

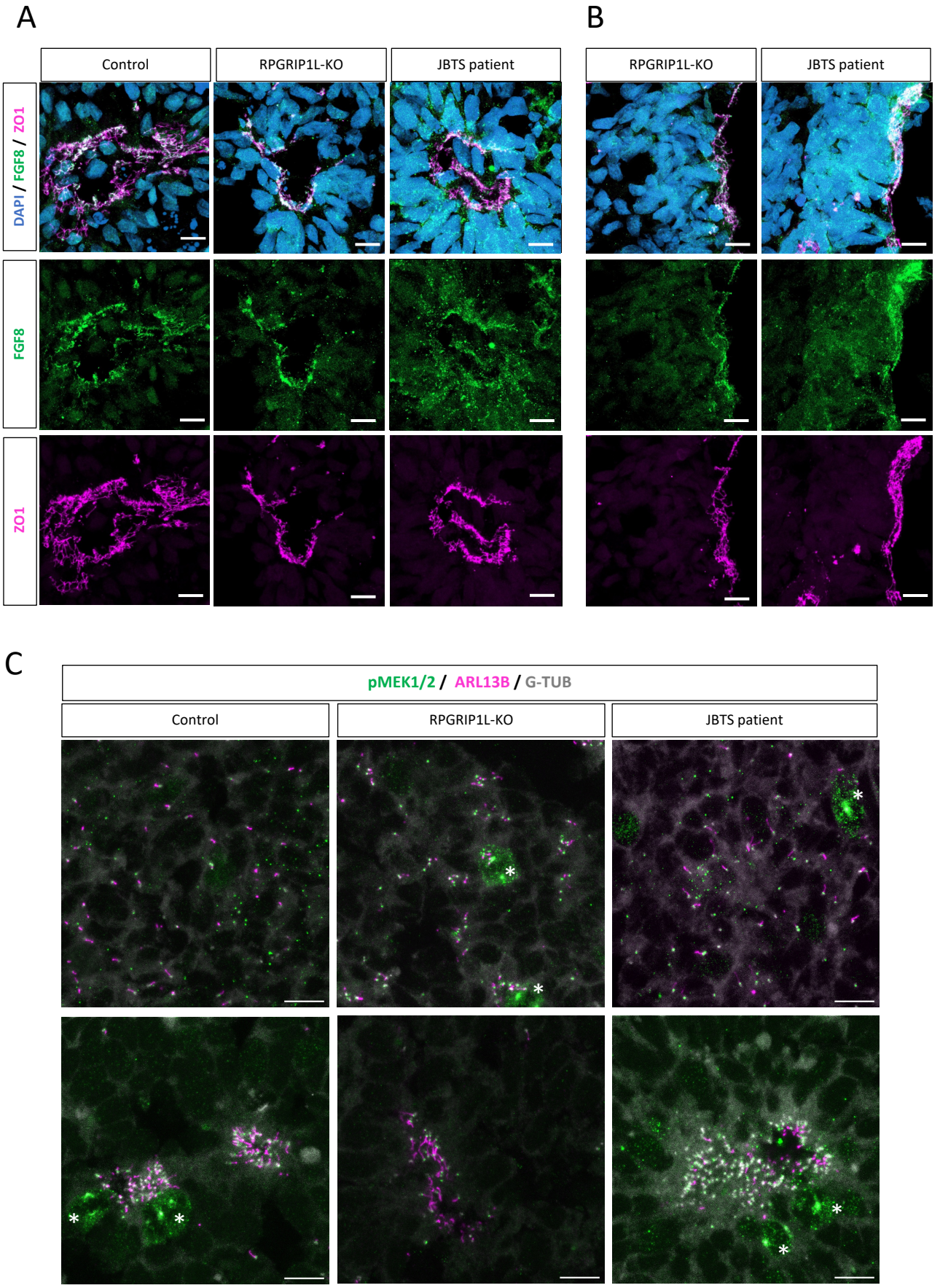

Figure 5

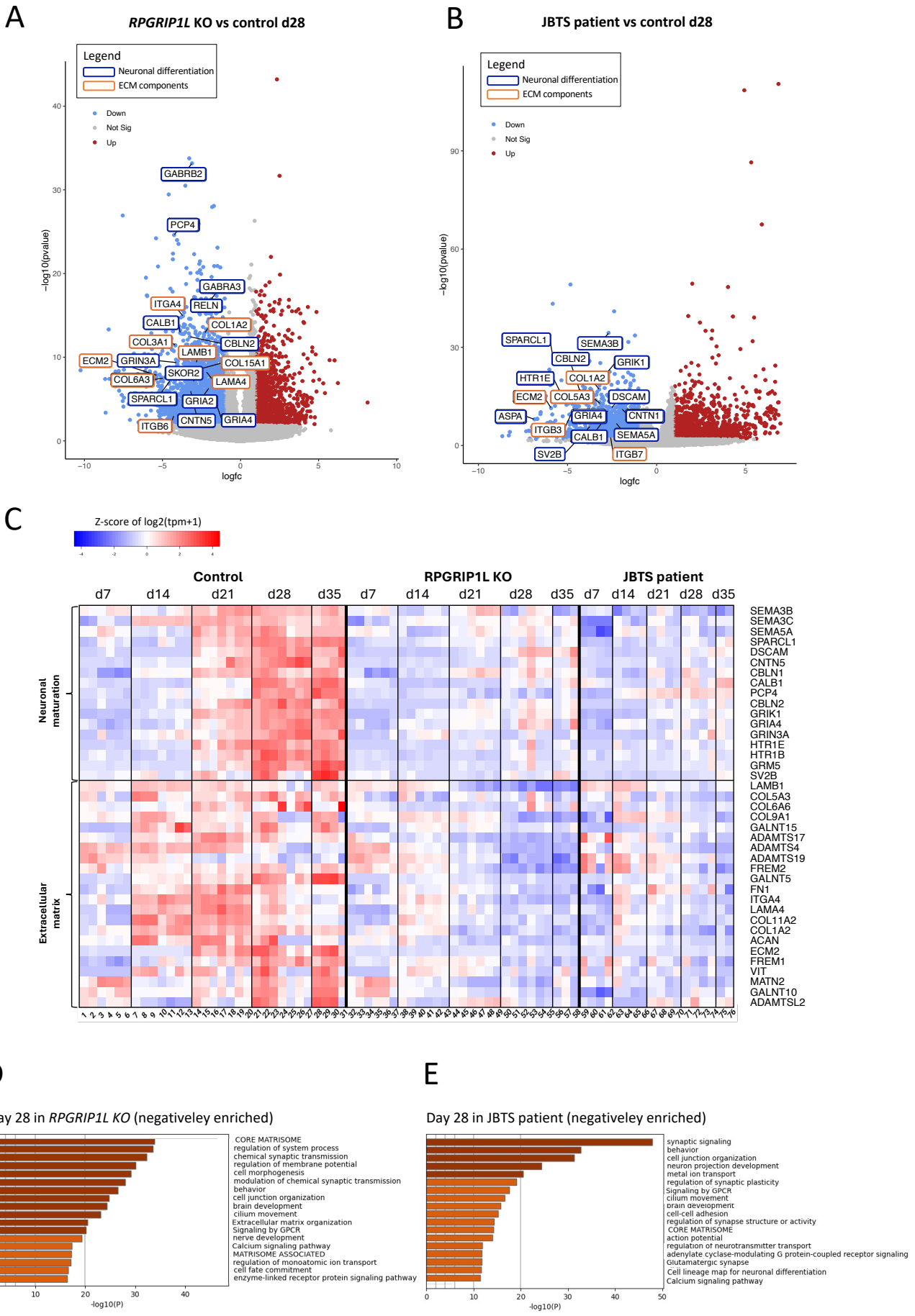
A
RPGRIP1L KO vs control d28
Legend
Neuronal differentiation
ECM components
Down
Not Sig
Up
GABRB2
PCP4
GABRA3
ITGA4
RELN
CALB1
COL1A2
COL3A1
CBLN2
LAMB1
ECM2
GRIN3A
COL15A1
SKOR2
COL6A3
LAMA4
SPARCL1
GRIA2
CNTN5
GRIA4
ITGB6
−log10(pvalue)
logfc
B
JBTS patient vs control d28
Legend
Neuronal differentiation
ECM components
Down
Not Sig
Up
SPARCL1
SEMA3B
CBLN2
GRIK1
HTR1E
COL1A2
ECM2
COL5A3
DSCAM
ASPA
GRIA4
CNTN1
ITGB3
CALB1
SEMA5A
SV2B
ITGB7
−log10(pvalue)
logfc
C
Z-score of log2(tpm+1)
Control
RPGRIP1L KO
JBTS patient
d7
d14
d21
d28
d35
Neuronal maturation
Extracellular matrix
SEMA3B
SEMA3C
SEMA5A
SPARCL1
DSCAM
CNTN5
CBLN1
CALB1
PCP4
CBLN2
GRIK1
GRIA4
GRIN3A
HTR1E
HTR1B
GRM5
SV2B
LAMB1
COL5A3
COL6A6
COL9A1
GALNT15
ADAMTS17
ADAMTS4
ADAMTS19
FREM2
GALNT5
FN1
ITGA4
LAMA4
COL11A2
COL1A2
ACAN
ECM2
FREM1
VIT
MATN2
GALNT10
ADAMTSL2
D
Day 28 in RPGRIP1L KO (negativeley enriched)
CORE MATRISOME
regulation of system process
chemical synaptic transmission
regulation of membrane potential
cell morphogenesis
modulation of chemical synaptic transmission
behavior
cell junction organization
brain development
cilium movement
Extracellular matrix organization
Signaling by GPCR
nerve development
Calcium signaling pathway
MATRISOME ASSOCIATED
regulation of monoatomic ion transport
cell fate commitment
enzyme-linked receptor protein signaling pathway
-log10(P)
E
Day 28 in JBTS patient (negativeley enriched)
synaptic signaling
behavior
cell junction organization
neuron projection development
metal ion transport
regulation of synaptic plasticity
Signaling by GPCR
cilium movement
brain development
cell-cell adhesion
regulation of synapse structure or activity
CORE MATRISOME
action potential
regulation of neurotransmitter transport
adenylate cyclase-modulating G protein-coupled receptor signaling
Glutamatergic synapse
Cell lineage map for neuronal differentiation
Calcium signaling pathway
-log10(P)

Figure 6

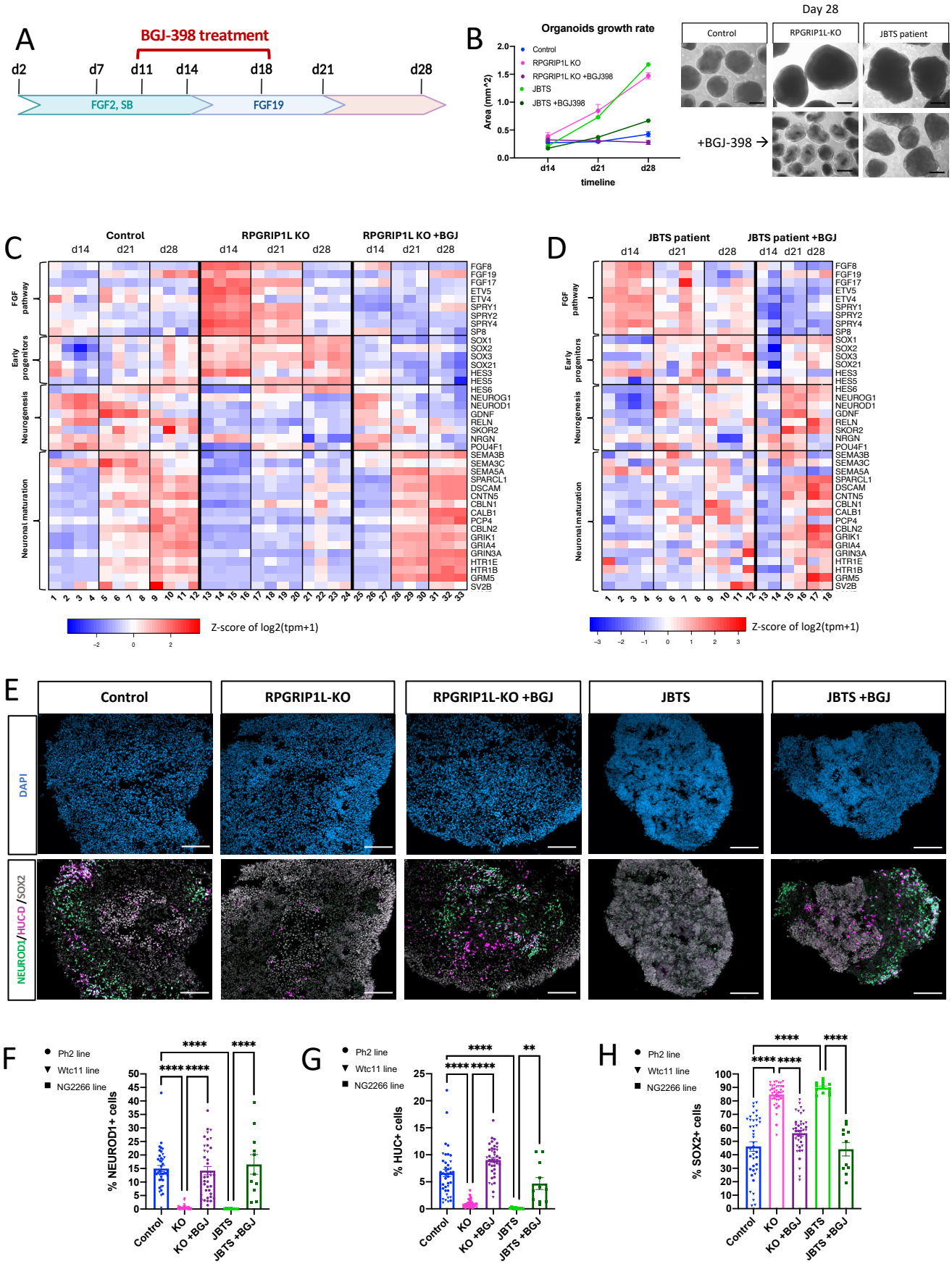
A
BGJ-398 treatment
d2
d7
d11
d14
d18
d21
d28
FGF2, SB
FGF19
B
Organoids growth rate
Control
RPGRIP1L KO
RPGRIP1L KO +BGJ398
JBTS
JBTS +BGJ398
Area (mm^2)
timeline
Day 28
Control
RPGRIP1L-KO
JBTS patient
+BGJ-398 →
C
Control
RPGRIP1L KO
RPGRIP1L KO +BGJ
d14
d21
d28
FGF pathway
Early progenitors
Neurogenesis
Neuronal maturation
FGF8
FGF19
FGF17
ETV5
ETV4
SPRY1
SPRY2
SPRY4
SP8
SOX1
SOX2
SOX3
SOX21
HES3
HES5
HES6
NEUROG1
NEUROD1
GDNF
RELN
SKOR2
NRGN
POU4F1
SEMA3B
SEMA3C
SEMA5A
SPARCL1
DSCAM
CNTN5
CBLN1
CALB1
PCP4
CBLN2
GRIK1
GRIA4
GRIN3A
HTR1E
HTR1B
GRM5
SV2B
Z-score of log2(tpm+1)
D
JBTS patient
JBTS patient +BGJ
E
Control
RPGRIP1L-KO
RPGRIP1L-KO +BGJ
JBTS
JBTS +BGJ
DAPI
NEUROD1/HUC-D /SOX2
F
Ph2 line
Wtc11 line
NG2266 line
% NEUROD1+ cells
Control
KO
KO +BGJ
JBTS
JBTS +BGJ
G
% HUC+ cells
H
% SOX2+ cells

Supplementary Figure 4

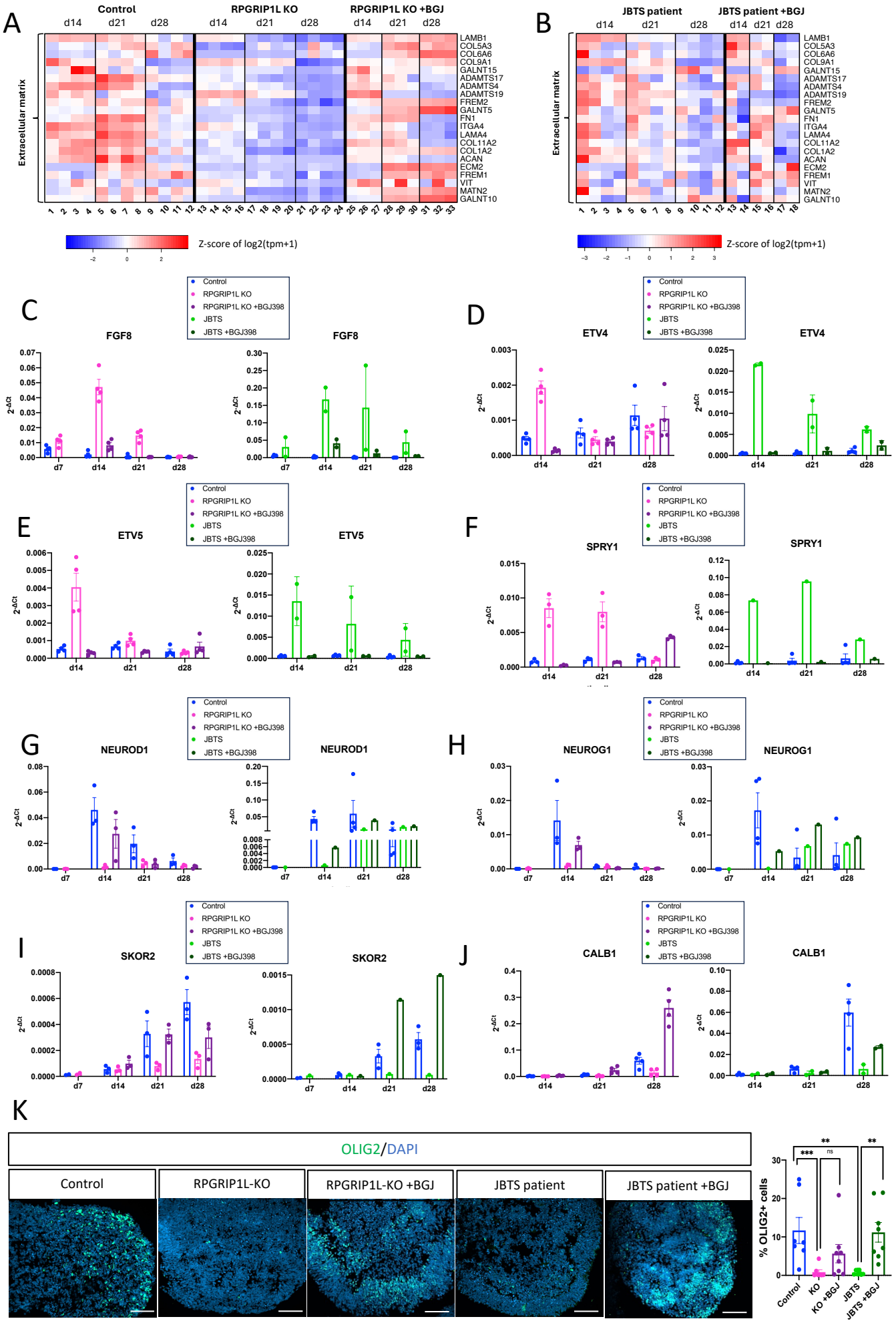

Figure 7

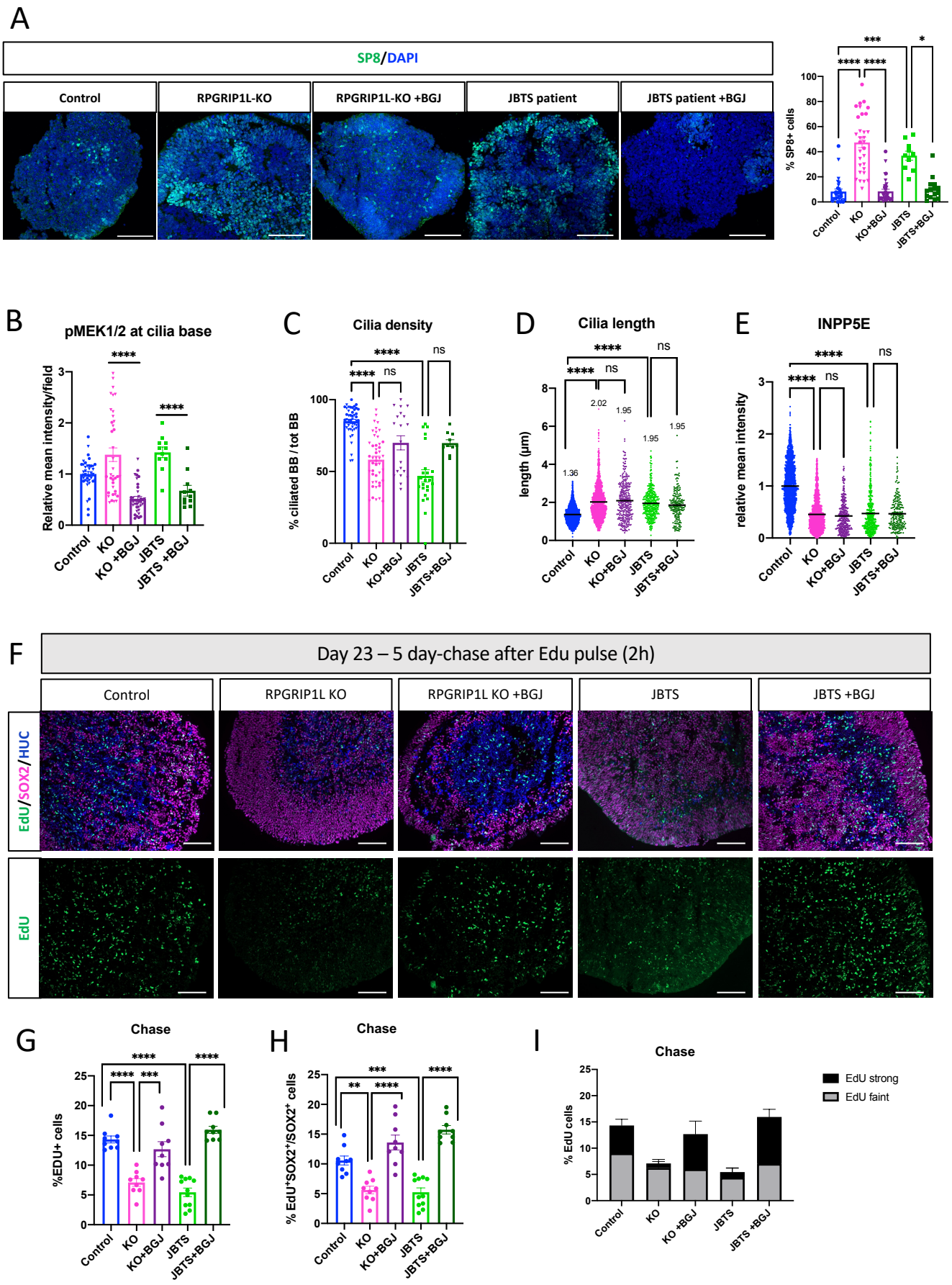
A
SP8/DAPI
Control
RPGRIP1L-KO
RPGRIP1L-KO +BGJ
JBTS patient
JBTS patient +BGJ
% SP8+ cells
Control
KO
KO+BGJ
JBTS
JBTS+BGJ
B
pMEK1/2 at cilia base
Relative mean intensity/field
KO +BGJ
JBTS +BGJ
C
Cilia density
% ciliated BB / tot BB
D
Cilia length
length (µm)
E
INPP5E
relative mean intensity
F
Day 23 – 5 day-chase after Edu pulse (2h)
RPGRIP1L KO
RPGRIP1L KO +BGJ
JBTS +BGJ
EdU/SOX2/HUC
EdU
G
Chase
%EDU+ cells
H
% EdU+SOX2+/SOX2+ cells
I
EdU strong
EdU faint
% EdU cells

Supplementary Figure 5

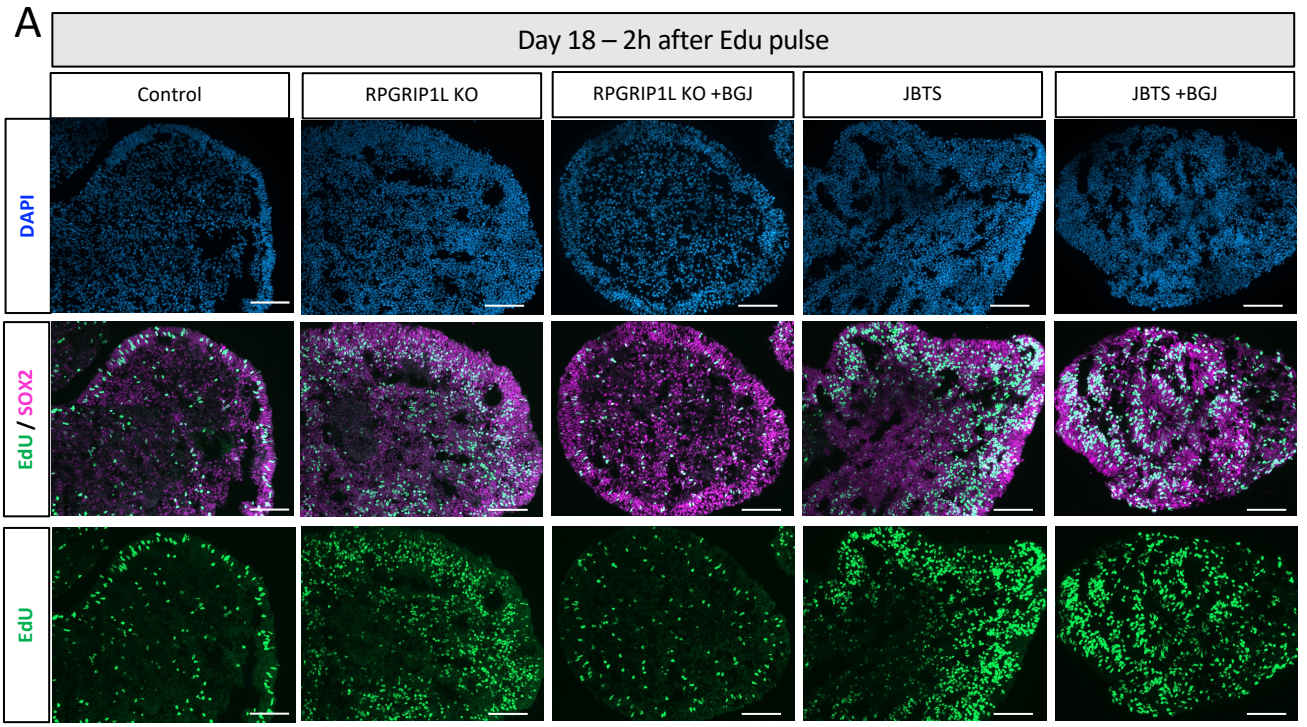

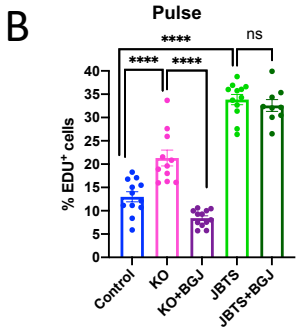

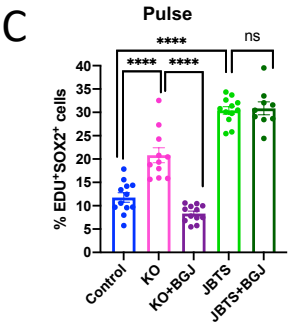
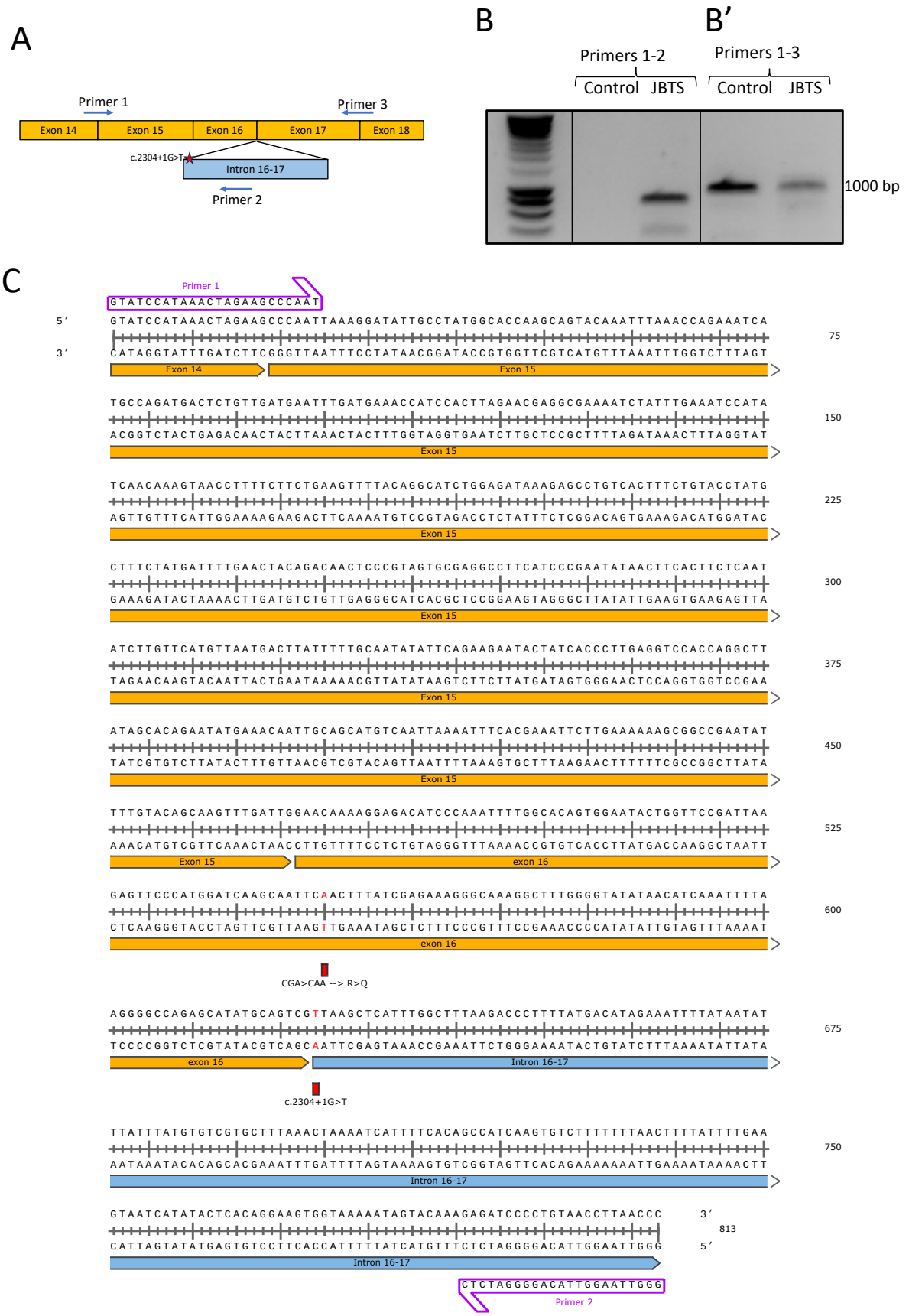
Supplementary Figure 6